Chapter 9
Higher-Dimensional Numerical Relativity: Current Status

Hirotaka Yoshino[1] and Masaru Shibata[2]

[1]*Cosmophysics Group, Institute of Particles and Nuclear Studies, KEK,
Tsukuba 305-0801, Japan*
[2]*Yukawa Institute for Theoretical Physics, Kyoto University,
Kyoto 606-8502, Japan*

We summarize the current status of numerical relativity for higher-dimensional space-times. In the first part, the ingredients necessary for successful simulations developed to date are summarized, including formulations, methods of implementing spacetime symmetries, and gauge conditions. In the second part, we review the simulations performed so far, such as time evolution of a black string that is unstable against the Gregory-Laflamme instability, black hole collisions and scatterings, and time evolution of rapidly rotating Myers-Perry (MP) black holes with one rotational parameter which are unstable against bar-mode deformation. The remaining issues and expected future developments are briefly described.

Contents

§1.   Introduction

Numerical relativity is probably the unique approach for a solution of dynamical problems in general relativity. In this approach, Einstein's equation,

$$G_{ab} = 8\pi G T_{ab}, \qquad (1\cdot1)$$

is numerically solved in the framework of an initial-value problem of general relativity. Numerical relativity for 4-dimensional (4D) spacetime has a very long history, and in particular in the past decade, its community achieved significant progress: Now, it is feasible to perform a longterm and accurate simulation for the merger of binary composed of black holes and neutron stars (e.g., Refs. 1)–6) for binary black holes and Ref. 7) for others) and for high-velocity collision of two black holes. These are among the strongest gravitational phenomena in nature.

High-dimensional numerical relativity is also being an important issue since the TeV gravity scenarios[8)–11)] and the AdS/CFT correspondence[12)] were proposed. To clarify nonlinear dynamics of higher-dimensional general relativity, numerical relativity for higher dimensions has to be developed. Higher-dimensional numerical relativity began in 2003 by a pioneering simulation for a 5-dimensional (5D) black string that is unstable against the Gregory-Laflamme instability.[13), 14)] Although history of higher-dimensional numerical relativity is not so long, several new formulations have been developed and several remarkable simulations have been performed in particular in the last three years. The purpose of this chapter is to review such formulations and new facts discovered by the latest simulations.

There are three primary motivations for performing higher-dimensional numerical relativity. The first one comes from the fact that mini black holes may be produced in large accelerators such as Large Hadron Collider (LHC) if the TeV gravity hypotheses are correct. If our 3-dimensional (3D) space is a D_3-brane in large[8), 9)] or warped[10)] extra dimensions, the Planck energy could be of $O(\text{TeV})$ and quantum gravity phenomena may emerge in high-energy particle colliders. If the particle energy is larger than the Planck energy in this scenario, mini black holes could be produced[15)–17)] (see also Ref. 18) for a recent review). If a black hole with mass energy slightly larger than the Planck energy is formed in the LHC, it will subsequently emit the Hawking radiation that may be detected. To accurately predict the rate of mini black-hole production and its detectability, it is necessary to know the cross section for the black-hole production σ_{BH}, and the resulting mass and angular momentum of the formed black hole. A lower bound for the black-hole production was given in Refs. 19) and 20) by numerically solving the apparent horizon at an instant of the collision of Aichelburg-Sexl particles[21)] in higher dimensions, by extending the analytic study[22)] of that system in 4 dimensions.[*)] However, the precise value of σ_{BH} and the black-hole production rate are necessary for precisely predicting the event rate in the particle collider.

The second motivation is to clarify the fundamental properties of black objects in higher dimensions. A 4D black hole (Kerr black hole) has been shown to be stable for vacuum spacetimes irrespective of the mass and spin. By contrast, higher-dimensional black objects are not always stable. For example, the Gregory-Laflamme instability[24)] is known for a black string. Also, higher-dimensional rapidly rotating black holes (i.e., the Myers-Perry (MP) black holes[25)]) are unstable,[26)–29)] and a

---

[*)] Because the apparent horizon formation implies the formation of the event horizon assuming the cosmic censorship (e.g., Ref. 23)), the cross section of the apparent horizon formation σ_{AH} gives the lower bound of σ_{BH} and thus lower bound for the production rate.

black hole on a Randall-Sundrum (RS) brane is also inferred to be unstable[30] (see also Chapters 6, 7, and 8 of this supplement). To clarify the condition for the onset of the instabilities and the final fate after their onset, numerical relativity plays a crucial role. Indeed, numerical relativity has discovered several dynamical instabilities (see §3).

The third motivation comes from the hypothesis of the AdS/CFT correspondence, which conjectures that the classical gravity of anti-de Sitter (AdS) spacetime is dual to the conformal field theory (CFT) on the boundary of the AdS spacetime. If this hypothesis holds, we are able to obtain an indication for a phenomena in CFT, for which explicit calculation is difficult due to strong coupling effect, by studying the dual gravitational system. One of the interesting phenomena predicted by the AdS/CFT correspondence is that a macroscopic black hole on a Randall-Sundrum (RS) brane could be unstable.[*] To answer this conjecture, numerical relativity will play an important role.

The purpose of this chapter is to overview the formulations and numerical methods developed so far, and numerical simulations performed by these implementations in higher-dimensional numerical relativity. This chapter is divided into two parts: The first part (§2) is devoted to reviewing formulations and techniques of higher-dimensional numerical relativity. The second part (§3) is devoted to reviewing numerical simulations performed so far.

This chapter is organized as follows. In §2, we review the three formulations for higher-dimensional numerical relativity (§2.1), the "cartoon methods" for implementing spacetime symmetries (§2.2), and the gauge conditions for fixing the coordinate conditions (§2.3), which are among the key ingredients for the successful simulations. Then, we briefly describe other necessary ingredients such as methods for extracting gravitational waves (§2.4), methods for finding an apparent horizon (§2.5), techniques for handling the black hole interior (§2.6), adaptive mesh refinement techniques (§2.7), and methods for preparing initial data (§2.8). We also summarize semi-analytic solutions that can be used for the benchmark tests to calibrate the reliability of numerical codes (§2.9).

In §3, we overview the simulations performed to date. In particular, we focus on reviewing numerical results for three types of simulations: Simulations of a black string that is unstable against the Gregory-Laflamme instability (§3.1), simulations of two black-hole collisions (§3.2), and simulations of rapidly rotating Myers-Perry (MP) black holes that may be unstable against nonaxisymmetric deformation (§3.3). In the second topic, we also review the simulations of high-velocity black-hole collisions in 4 dimensions (§3.2.2) as well as slow-velocity black-hole collisions in higher dimensions (§3.2.1) because these are related topics.

§4 is devoted to a summary. The issues for the future are briefly discussed.

Notations and Conventions

Thoroughout this chapter, the unit $c = 1$ is used, while the higher-dimensional

---

[*] If we assume that the AdS/CFT correspondence is held in a RS brane spacetime, a 5D classical black hole on the RS brane is expected to be dual to a 4D black hole with quantum fields[31], [32] (see Chapter 8).

gravitational constant G is explicitly shown. The dimensionality of a spacelike hypersurface in a D-dimensional spacetime is written as N, i.e. $D = N + 1$. The line element and the area of an n-dimensional unit sphere are denoted as $d\Omega_n^2$ and Ω_n, respectively, where $\Omega_n = 2\pi^{(n+1)/2}\Gamma((n + 1)/2)$. The horizon radius of a Schwarzschild-Tangherlini black hole is denoted as r_S, where $r_S^{D-3} = \frac{16\pi GM}{(D-2)\Omega_{D-2}}$.

§2.   Formulations and techniques

In this section, we overview the formulations and numerical methods for simulating higher-dimensional spacetimes that have been developed to date. The ingredients necessary for a simulation of vacuum spacetime in numerical relativity are listed up as follows:

- Formulations, including methods for implementing spacetime symmetries for a special class of spacetime;
- Appropriate gauge conditions;
- Methods for extracting gravitational waves;
- Techniques for handling the black hole interior;
- Apparent horizon finder;
- Adaptive mesh refinement (AMR);
- Methods for preparing initial data.

For the development of these ingredients, there is a long history in 4D numerical relativity. Although some of them can be extended for higher-dimensional numerical relativity in a straightforward manner, a nontrivial extension is required for many of them. We describe the methods of extension one by one in the following subsections. In addition, we summarize

- (Semi)analytic solutions available for benchmark tests

that can be used for calibrating the codes newly developed.

2.1.   *Formulation*

In numerical relativity, Einstein's equation is solved as the initial value problem using the so-called $N+1$ formalism where $N = D - 1$ is the spatial dimensionality and D the spacetime one. $N+1$ formalism in numerical relativity has to enable a stable numerical computation; a small numerical error associated with numerical truncation error should not grow in time. The well-known initial-value formalism of Einstein's equation is the Arnowitt-Deser-Misner (ADM) formalism.[33] However, it turns out that it is not suitable for numerical-relativity simulation and cannot be used for longterm simulations (although it may be applied to short-term simulations).

In 4D numerical relativity, two robust formalisms have been developed and used for simulating black hole spacetimes: The generalized harmonic (GH)[34] and the Baumgarte-Shapiro-Shibata-Nakamura (BSSN) formalisms.[35],[36] The GH formalism can be straightforwardly extended for a use of higher-dimensional numerical relativity. The BSSN formalism was also extended with slight modifications.[37] In addition, the method of 4D reduction (i.e. $4 + (D - 4)$ splitting) was proposed for simulating spacetimes of $O(D - 3)$ symmetry,[38] which is an extension of 2+1+1 formalism in 4D numerical relativity.[39] In the following, we review these three

methods one by one.

2.1.1. Generalized harmonic formalism

The GH formalism was originally proposed by Garfinkle.[34] Here, we briefly summarize this method. Although this was originally developed for 4D numerical relativity, the same formulation may be used for arbitrary dimensionality with minor modification.

In the GH formalism, Einstein's equation is written in a hyperbolic manner as often done in the post-Newtonian study and the generalized harmonic gauge condition is imposed introducing an auxiliary D-dimensional function H^I as

$$H^I = \Box x^I = \frac{1}{\sqrt{-g}} \partial_J \left(\sqrt{-g} g^{JI} \right), \tag{2·1}$$

where $I = 0,...,N$ and each coordinate x^I is regarded as a scalar function. Then, Einstein's equation $R_{IJ} = 8\pi G[T_{IJ} - g_{IJ}T/(D-2)]$ is rewritten as

$$g^{KL}g_{IJ,KL} + g^{KL}_{,J}g_{IL,K} + g^{KL}_{,I}g_{JL,K} + 2H_{(I,J)} - 2H_L\Gamma^L_{IJ} + 2\Gamma^K_{IJ}\Gamma^L_{KI}$$
$$= -16\pi G[T_{IJ} - Tg_{IJ}/(D-2)], \tag{2·2}$$

where $H_I = g_{IJ}H^J$.

Appropriate choice of the gauge variable H^I is the key for stable and accurate numerical simulation. In Ref. 40), several candidates for the gauge conditions are proposed. In the study of the Gregory-Laflamme instability by Lehner and Pretorius,[41] the Cartesian-type coordinates are used and the simple condition

$$H^I = 0 \tag{2·3}$$

was imposed, which often enables a stable numerical simulation.

On the other hand, in the axisymmetric $(2+1$ dimensional) simulation[42] of complex scalar fields minimally coupled to gravity in D-dimensional Kaluza-Klein spacetimes by Sorkin, the cylindrical-type coordinates are used and the variant of the damped-wave gauge condition[43] was adopted.

2.1.2. Higher-dimensional BSSN formalism

In 4D numerical relativity, the BSSN formalism[35),36)] is most popular. Extension to higher-dimensional numerical relativity is also straightforward.[37] The BSSN formalism is in a sense a modified version of the ADM formalism; the numerical stability is realized by a suitable modification of the ADM formalism. In the following, we briefly review the ADM formalism and the BSSN formalism for D-dimensional spacetime.

Suppose $\mathcal{M}$ be a D-dimensional spacetime with a metric g_{ab}. Consider a sequence of N-dimensional spacelike hypersurfaces $\Sigma_t(h_{ab}, K_{ab})$ foliated by a time coordinate t in $\mathcal{M}$. Here, h_{ab} is the induced metric $h_{ab} := g_{ab} + n_a n_b$ of Σ_t, where n_a is the future-directed unit normal Σ_t, and K_{ab} is the extrinsic curvature defined by $K_{ab} := -(1/2)\pounds_n h_{ab}$, where $\pounds_n$ is the Lie derivative with respect to n^a. The coordinate basis t^a of the time coordinate t is decomposed as $t^a = \alpha n^a + \beta^a$, where

α and β^a are the lapse function and the shift vector, respectively. In terms of these variables, Einstein's equation is rewritten as

$$R + K^2 - K_{ab}K^{ab} = 16\pi G\rho, \tag{2.4}$$

$$D_b K^b_{\ a} - D_a K = 8\pi G j_a, \tag{2.5}$$

$$\pounds_t h_{ab} = -2\alpha K_{ab} + D_a\beta_b + D_b\beta_a, \tag{2.6}$$

$$\pounds_t K_{ab} = -D_a D_b \alpha + \alpha \left(R^{(\Sigma)}_{ab} - 2K_{ac}K^c_{\ b} + K_{ab}K \right)$$
$$+ \beta^c D_c K_{ab} + K_{cb}D_a\beta^c + K_{ca}D_b\beta^c - 8\pi G\alpha \left[S_{ab} + \frac{\rho - S}{D - 2}h_{ab} \right], \tag{2.7}$$

where Eq. (2.6) is equivalent to the definition of K_{ab}, and Eqs. (2.4), (2.5), and (2.7) are derived from $G_{ab}n^a n^b = 8\pi G\rho$, $G_{bc}n^b h^c_{\ a} = -8\pi G j_a$, and $G_{cd}h^c_{\ a}h^d_{\ b} = 8\pi S_{ab}$ using Gauss, Codacci, and Ricci equations, respectively. Here, we defined

$$\rho := T_{ab}n^a n^b; \qquad j_a := -T_{bc}n^b h^c_{\ a}; \qquad S_{ab} := T_{cd}h^c_{\ a}h^d_{\ b}, \tag{2.8}$$

and $S := S^c_{\ c}$. $R^{(\Sigma)}_{ab}$ denotes the Ricci tensor with respect to h_{ab}.

Equations (2.4) and (2.5) are Hamiltonian and momentum constraint equations. The initial spacelike hypersurface (i.e., initial data) has to be prepared so that these two constraints are satisfied. Then, the time evolution of (h_{ab}, K_{ab}) is determined by Eqs. (2.6) and (2.7). The constraint equations are automatically satisfied after the time evolution as long as the evolution equations are solved exactly. However, these constraints are always violated slightly in actual simulations, although the violation does not grow in an appropriate formulation.

The expressions shown above are given in terms of the abstract index notation. Introducing the coordinates x^i that span the hypersurface Σ_t, the line element is written as

$$ds^2 = -\alpha^2 dt^2 + h_{ij}(dx^i + \beta^i dt)(dx^j + \beta^j dt), \tag{2.9}$$

and the spatial components h^{ij} of h^{ab} are the inverse of h_{ij}. The equations expressed in terms of x^i are obtained by replacing the indices a, b to the spatial indices i, j and the Lie derivative $\pounds_t$ to the coordinate derivative ∂_t. In the following, we assume to use the Cartesian coordinates.

Next, the higher-dimensional version of the BSSN formalism is reviewed. The basic idea of the BSSN formalism is to increase the number of variables as well as that of constraints to suppress the growth of unphysical modes that may grow due to truncation error associated with the finite difference. Specifically, new variables, χ, $\tilde{h}_{ij}$, $\tilde{A}_{ij}$, and $\tilde{\Gamma}^i$, are introduced:

$$\tilde{h}_{ij} = \chi h_{ij}, \quad K_{ij} = \frac{1}{\chi}\left(\tilde{A}_{ij} + \frac{K}{N}\tilde{h}_{ij} \right), \quad \tilde{\Gamma}^i := h^{jk}\tilde{\Gamma}^i_{jk} = -\tilde{h}^{ik}_{\ \ ,k}. \tag{2.10}$$

Here, the conformal factor χ is chosen so that the determinant $\tilde{h}$ of $\tilde{h}_{ij}$ satisfies the condition

$$\tilde{h} = 1, \tag{2.11}$$

which is equivalent to setting $\chi = h^{-1/N}$, and $\tilde{\Gamma}^i_{jk}$ denotes the Christoffel symbol with respect to $\tilde{h}_{ij}$. The evolution equations are derived as

$$(\partial_t - \beta^i \partial_i)\chi = \frac{2}{N}\chi\left(\alpha K - \partial_i \beta^i\right), \tag{2.12}$$

$$(\partial_t - \beta^i \partial_i)K = -D_i D^i \alpha + \alpha\left(\tilde{A}^{ij}\tilde{A}_{ij} + \frac{K^2}{N}\right) + \frac{8\pi\alpha}{D-2}\left[(D-3)\rho + S\right], \tag{2.13}$$

$$(\partial_t - \beta^j \partial_j)\tilde{\Gamma}^i = -2\tilde{A}^{ij}\partial_j\alpha + 2\alpha\left[\tilde{\Gamma}^i_{jk}\tilde{A}^{jk} - \frac{D-2}{N}\tilde{h}^{ij}K_{,j} - 8\pi\tilde{h}^{ij}j_j - \frac{N\chi_{,j}}{2\chi}\tilde{A}^{ij}\right]$$
$$- \tilde{\Gamma}^j \partial_j\beta^i + \frac{2}{N}\tilde{\Gamma}^i \partial_j\beta^j + \frac{D-3}{N}\tilde{h}^{ik}\beta^j_{,jk} + \tilde{h}^{jk}\beta^i_{,jk}. \tag{2.14}$$

$$(\partial_t - \beta^k \partial_k)\tilde{h}_{ij} = -2\alpha\tilde{A}_{ij} + \tilde{h}_{ik}\partial_j\beta^k + \tilde{h}_{jk}\partial_i\beta^k - \frac{2}{N}\partial_k\beta^k\tilde{h}_{ij}, \tag{2.15}$$

$$(\partial_t - \beta^k \partial_k)\tilde{A}_{ij} = \chi\left[-(D_i D_j \alpha)^{\text{TF}} + \alpha\left(R^{(\Sigma)\text{TF}}_{ij} - 8\pi S^{\text{TF}}_{ij}\right)\right]$$
$$+ \alpha\left(K\tilde{A}_{ij} - 2\tilde{A}_{ik}\tilde{A}^k_j\right) + \tilde{A}_{ik}\partial_j\beta^k + \tilde{A}_{kj}\partial_i\beta^k - \frac{2}{N}\partial_k\beta^k\tilde{A}_{ij}, \tag{2.16}$$

where the indices of $\tilde{A}_{ij}$ are raised and lowered by $\tilde{h}_{ij}$, and TF denotes the trace-free part, e.g., $R^{(\Sigma)\text{TF}}_{ij} = R^{(\Sigma)}_{ij} - R^{(\Sigma)}h_{ij}/N$. The Ricci tensor is decomposed into two parts as

$$R^{(\Sigma)}_{ij} = \tilde{R}_{ij} + R^{(\chi)}_{ij}, \tag{2.17}$$

where $\tilde{R}_{ij}$ is the Ricci tensor with respect to $\tilde{h}_{ij}$ and $R^{(\chi)}_{ij}$ is the contribution of the conformal factor. They are written as

$$\tilde{R}_{ij} = -\frac{1}{2}\tilde{h}^{kl}\tilde{h}_{ij,kl} + \frac{1}{2}\left(\tilde{h}_{ki}\partial_j\tilde{\Gamma}^k + \tilde{h}_{kj}\partial_i\tilde{\Gamma}^k\right)$$
$$-\frac{1}{2}\left(\tilde{h}_{il,k}\tilde{h}^{kl}{}_{,j} + \tilde{h}_{jl,k}\tilde{h}^{kl}{}_{,i} - \tilde{\Gamma}^l\tilde{h}_{ij,l}\right) - \tilde{\Gamma}^l_{ik}\tilde{\Gamma}^k_{jl}, \tag{2.18}$$

$$R^{(\chi)}_{ij} = \frac{(D-3)}{2\chi}\left(\chi_{,ij} - \tilde{\Gamma}^k_{ij}\chi_{,k}\right) - \frac{(D-3)}{4}\frac{\chi_{,i}\chi_{,j}}{\chi^2}$$
$$+ \tilde{h}_{ij}\tilde{h}^{kl}\left[\frac{\chi_{,kl}}{2\chi} - \frac{N\chi_{,k}\chi_{,l}}{4\chi^2}\right] - \frac{1}{2}\tilde{h}_{ij}\frac{\chi_{,m}}{\chi}\tilde{\Gamma}^m. \tag{2.19}$$

The second derivatives of $\tilde{h}_{ij}$ appear only in the first term of Eq. (2.18) (i.e., each component of h_{ij} appears to obey a simple wave equation) and this is the key point for the numerical stability.

In summary, the variables to be evolved are χ, K, $\tilde{h}_{ij}$, $\tilde{A}_{ij}$ and $\tilde{\Gamma}^i$, and they follow Eqs. (2.12), (2.13), (2.15), (2.16), and (2.14), respectively. The conditions $\tilde{A}^i{}_i = 0$, third equation of Eq. (2.10), and Eq. (2.11) are regarded as the new constraints which arise because the number of the dynamical variables are increased. As shown above, the BSSN formalism for higher dimensions has essentially the same form as that for the 4D case, except that some coefficients are changed.

2.1.3. $4 + (D - 4)$ split

The third formulation is the $4 + (D - 4)$ splitting method developed by Zilhao et al.[38] The idea is essentially the same as that for the $(2 + 1) + 1$ formalism for axisymmetric systems in the 4D numerical relativity.[39] Both formalisms are derived extending a dimensional-reduction formalism developed by Geroch.[44] In the following, we briefly summarize this dimensional reduction technique.

As assumed in Ref. 38), we here only consider the spacetimes of $O(D - 3)$ symmetry in which there is a 3D hyperplane (spanned by (t, x, y)) in D dimensions, and the remaining $(D - 3)$ directions (spanned by $(z, w_1, ..., w_{D-4})$) orthogonal to the 3D hyperplane have symmetries of rotations and reflection with respect to any point (t, x, y) in this hyperplane. The $O(D - 3)$ symmetry is the same as $SO(D - 3)$ symmetry (i.e., symmetry only of rotations) for $D \geq 6$, but it is a symmetry larger than the $SO(D-3)$ for $D = 5$ because the reflection symmetry excludes any rotating system along the symmetric direction. In this symmetry, it is proven that the metric can be reduced to the form

$$ds^2 = g_{\mu\nu}dx^\mu dx^\nu + \lambda(x^\mu)d\Omega_{D-4}^2, \qquad (2\cdot20)$$

where $d\Omega_{D-4}^2$ is the metric of a $(D - 4)$-dimensional unit sphere and $\mu, \nu = 0,...,3$ (i.e., $x^\mu = t, x, y, z$). Then, Einstein's equation for vacuum is written as

$$R_{\mu\nu} = \frac{D - 4}{2\lambda}\left(\nabla_\mu\nabla_\nu\lambda - \frac{1}{2\lambda}\nabla_\mu\lambda\nabla_\nu\lambda\right), \qquad (2\cdot21)$$

$$\nabla^\mu\nabla_\mu\lambda = 2(D - 5) - \frac{D - 6}{2\lambda}\nabla_\mu\lambda\nabla^\mu\lambda, \qquad (2\cdot22)$$

where ∇_μ is the covariant derivative with respect to $g_{\mu\nu}$. These equations are effectively 4D Einstein's equation for $g_{\mu\nu}$ coupled to a scalar field $\lambda(x^\mu)$, and therefore, can be evolved using the standard BSSN formalism for 4 dimensions.

Note that the metric ansatz (2·20) can be applied also to spacetimes of symmetry $O(D - 2)$ that is a symmetry group larger than $O(D - 3)$, although in this case not all symmetries are manifest in the ansatz. An $O(D - 2)$-symmetric spacetime is similar to an axisymmetric 4D spacetime in the sense that in both cases there is a 1-dimensional (1D) symmetric axis of which orthogonal spatial directions have the same structure. In Refs. 38), 45) and 46), $O(D - 2)$-symmetric systems were simulated using this formulation.

2.2. *Implementing spacetime symmetries*

When some symmetries may be assumed to be present in a spacetime to simulate, such symmetries should be imposed in numerical simulation to reduce computational costs. Among three formulations summarized in the previous subsection, the BSSN formalism was described assuming the use of the Cartesian coordinates without assuming the presence of any symmetries a priori. In this subsection, we describe the so-called cartoon method for imposing symmetries in such a formalism.

2.2.1. Cartoon method

The cartoon method was originally proposed by Alcubierre et al.[47] as a robust prescription for an efficient numerical simulation of axisymmetric 4D spacetimes.

The essence in this method is to employ not curvilinear coordinates that possess coordinate singularities, but the Cartesian coordinates. First of all, we briefly review the original idea of the cartoon method.

In an axisymmetric 3D space, the Cartesian coordinates (x, y, z) are introduced so that the z axis becomes the symmetry axis of axisymmetry ($U(1)$ symmetry) (we refer to this case as "$x = y$, z" which indicates that the spatial structures in the x and y directions are equivalent). In the Cartesian coordinates, the $U(1)$ symmetry does not explicitly appear in equations, and we cannot evolve the geometric variables straightforwardly only with the data on, e.g., the (x, z)-plane because y derivatives of them are needed. In the originally cartoon method, a few grid points in the neighborhood of the (x, z)-plane are prepared. Then, the data at a grid point $(x, y \neq 0, z)$ is generated using the data at a point $(\rho, 0, z)$ (i.e. on the (x, z)-plane) where $\rho = \sqrt{x^2 + y^2}$, using the $U(1)$ symmetry. Here, an appropriate interpolation has to be done because the point $(\rho, 0, z)$ is not located on a grid in general. Once the data at the grid points $y \neq 0$ are known, y derivatives at $y = 0$ are calculated and the data on the (x, z)-plane is evolved toward the next time step.

The symmetric relations are derived as

$$\alpha(x, y, z) = \alpha(\rho, 0, z), \tag{2·23}$$

$$\beta^x(x, y, z) = (x/\rho)\beta^x(\rho, 0, z) - (y/\rho)\beta^y(\rho, 0, z), \tag{2·24}$$

$$\beta^y(x, y, z) = (y/\rho)\beta^x(\rho, 0, z) + (x/\rho)\beta^y(\rho, 0, z), \tag{2·25}$$

$$S_{xx}(x, y, z) = (x/\rho)^2 S_{xx}(\rho, 0, z) + (y/\rho)^2 S_{yy}(\rho, 0, z) - (2xy/\rho^2)S_{xy}(\rho, 0, z), \tag{2·26}$$

$$S_{yy}(x, y, z) = (y/\rho)^2 S_{xx}(\rho, 0, z) + (x/\rho)^2 S_{yy}(\rho, 0, z) + (2xy/\rho^2)S_{xy}(\rho, 0, z), \tag{2·27}$$

$$S_{xy}(x, y, z) = (xy/\rho^2)\left[S_{xx}(\rho, 0, z) - S_{yy}(\rho, 0, z)\right] + [(x^2 - y^2)/\rho^2]S_{xy}(\rho, 0, z), \tag{2·28}$$

for a scalar, a vector, and a symmetric tensor, using the fact that the Lie derivative of the functions with respect to the Killing vector becomes zero.

In Ref. 37), Yoshino and Shibata discussed the extensions of the cartoon method to 5D spacetimes (4D spaces) in the cases of three types of symmetries, i.e., the $U(1)$ symmetry ("x, y, $z = w$"), the $U(1) \times U(1)$ symmetry ("$x = y$, $z = w$"), and the $O(3)$ symmetry ("$x = y = z$, w") denoting the Cartesian coordinates by (x, y, z, w). For the $U(1)$ symmetry, the extension is straightforwardly done. The cartoon method for the $U(1) \times U(1)$ symmetry is similar to that for the $U(1)$ symmetric case except that two cartoons are required in this case. In the case of the $SO(3)$ symmetry, the symmetric relations are different from that for the $U(1)$ symmetric case, but they can be derived in a similar manner (see Ref. 37) for details).

2.2.2. Modified cartoon method

In the above straightforward extension of the cartoon method for the higher dimensional spacetimes, we have to prepare the extra grids in all the symmetric directions. For this reason, as the dimensionality D is increased by 1, the required grid number always increases by a factor of 5 (in the fourth-order finite differencing),

and thus, a lot of memories are still required for a large value of D. However, this can be avoided by a prescription shown below.[29)]

As an example, we here consider an N-dimensional space with the coordinates $(x, y, z, w_1, ..., w_n)$ where $n = D-4$, and suppose that this space has $O(D-3)$ symmetry with respect to $(z, w_1, ..., w_n)$ (i.e., "$z = w_1 = \cdots = w_n$"). The simulation is supposed to be performed on the (x, y, z)-plane. Here, we introduce $\rho = \sqrt{z^2 + \sum_i w_i^2}$, and in the following, indices a and b denote x or y. The symmetric relation of a scalar function is

$$\alpha(x, y, z, w_i) = \alpha(x, y, \rho, 0), \tag{2.29}$$

and from this relation, the derivatives are evaluated as

$$\alpha_{,w_i} = \alpha_{,aw_i} = \alpha_{,zw_i} = 0, \quad \alpha_{,w_i w_j} = (\alpha_{,z}/z)\delta_{ij}. \tag{2.30}$$

As for a vector function β^i, the x and y components of β^a have the same symmetric relations as the scalar function, and the symmetric relations of the z and w^i components are

$$\beta^z(x, y, z, w_i) = (z/\rho)\beta^z(x, y, \rho, 0), \tag{2.31}$$

$$\beta^{w_i}(x, y, z, w_i) = (w_i/\rho)\beta^z(x, y, \rho, 0), \tag{2.32}$$

and thus, we have

$$\beta^z_{,w_i} = \beta^{w_i}_{,a} = \beta^{w_i}_{,z} = \beta^z_{,aw_i} = \beta^z_{,zw_i} = \beta^{w_i}_{,ab} = \beta^{w_i}_{,az} = \beta^{w_i}_{,w_j w_k} = 0, \tag{2.33}$$

$$\beta^{w_i}_{,w_j} = (\beta^z/z)\delta_{ij}, \quad \beta^{w_i}_{,aw_j} = (\beta^z_{,a}/z)\delta_{ij}, \quad \beta^z_{,w_i w_j} = \beta^{w_i}_{,zw_j} = (1/z)\left(\beta^z_{,z} - \beta^z/z\right)\delta_{ij}. \tag{2.34}$$

As for a symmetric tensor function $S_{ij} = S_{ji}$, the components S_{ab} have the same symmetric relations as the scalar function, and (S_{az}, S_{aw_i}) have the same symmetric relations as the (z, w_i) components of the vector function. The symmetric relations of the other components are

$$S_{zz}(x, y, z, w_i) = \left(z^2/\rho^2\right) S_{zz}(x, y, \rho, 0) + \left(1 - z^2/\rho^2\right) S_{ww}(x, y, \rho, 0), \tag{2.35}$$

$$S_{w_i w_i}(x, y, z, w_i) = \left(w_i^2/\rho^2\right) S_{zz}(x, y, \rho, 0) + \left(1 - w_i^2/\rho^2\right) S_{ww}(x, y, \rho, 0), \tag{2.36}$$

$$S_{zw_i}(x, y, z, w_i) = \left(zw_i/\rho^2\right) \left[S_{zz}(x, y, \rho, 0) - S_{ww}(x, y, \rho, 0)\right], \tag{2.37}$$

$$S_{w_i w_j}(x, y, z, w_i) = \left(w_i w_j/\rho^2\right) \left[S_{zz}(x, y, \rho, 0) - S_{ww}(x, y, \rho, 0)\right], \quad (i \neq j). \tag{2.38}$$

From these relations, we have

$$S_{zz,w_i} = S_{w_i w_i, w_j} = S_{zw_i, a} = S_{zw_i, z} = S_{zz, aw_i} = S_{zz, zw_i}$$
$$= S_{w_i w_i, aw_j} = S_{w_i w_i, zw_j} = S_{zw_i, ab} = S_{zw_i, az} = S_{zw_i, zz} = 0, \tag{2.39}$$

$$S_{w_i w_j, a} = S_{w_i w_j, z} = S_{w_i w_j, w_k} = S_{w_i w_j, ab} = S_{w_i w_j, az}$$
$$= S_{w_i w_j, zz} = S_{w_i w_j, aw_k} = S_{w_i w_j, zw_k} = 0, (i \neq j), \tag{2.40}$$

$$S_{zw_i,w_j} = (1/z)\left(S_{zz} - S_{ww}\right)\delta_{ij}, \quad S_{zw_i,aw_j} = (1/z)\left(S_{zz,a} - S_{ww,a}\right)\delta_{ij}, \qquad (2\cdot41)$$

$$S_{zz,w_iw_j} = (1/z)\left[S_{zz,z} + (2/z)\left(S_{ww} - S_{zz}\right)\right]\delta_{ij}, \qquad (2\cdot42)$$

$$S_{w_iw_i,w_jw_k} = (2/z^2)\delta_{ik}\delta_{ij}\left(S_{zz} - S_{ww}\right) + (S_{ww,z}/z)\delta_{jk}, \qquad (2\cdot43)$$

$$S_{zw_i,zw_j} = (1/z)\left[S_{zz,z} - S_{ww,z} - (1/z)\left(S_{zz} - S_{ww}\right)\right]\delta_{ij}, \qquad (2\cdot44)$$

$$S_{w_iw_j,w_kw_l} = (1/z^2)\left(\delta_{il}\delta_{jk} + \delta_{ik}\delta_{jl}\right)\left(S_{zz} - S_{ww}\right), \quad (i \neq j). \qquad (2\cdot45)$$

Using these formulas, all the derivatives necessary for solving the evolution equations can be evaluated without preparing the extra grids and the simulation is effectively performed in the 3+1 manner.

2.3. *Gauge conditions*

General relativity is a covariant theory and thus there is a degree of freedom for choosing the coordinates. In numerical relativity, the choice of the coordinate conditions (or the choice of the conditions for the lapse function α and the shift vector β^i) is crucial for a stable and longterm simulation. The gauge conditions in the GH formalism were already reviewed in §2.1.1. Here, we describe popular gauge conditions in the BSSN formalism.

In 1970's, the maximal slicing condition $K = 0$ and the minimal distortion gauge[48] were proposed as one of the best sets of the gauge conditions. The reason is that the maximal slicing condition makes the spacelike hypersurface avoid the spacelike singularity of a spacetime in the presence of a black hole, and the minimal distortion gauge suppresses the distortion of coordinates as much as possible. The shortcoming in this approach is that elliptic equations have to be solved in each time step, which is computationally expensive. As an alternative set for the gauge condition which effectively realizes the above conditions, the dynamical time slicing condition[49] (or often called the $1 + \log$ condition) and the Γ-driver condition[50] were recently proposed and employed.[*] In this condition, the following equations are solved

$$\partial_t \alpha - \beta^i \partial_i \alpha = -2\alpha K, \qquad (2\cdot46)$$

$$\partial_t \beta^i = (3/4)B^i, \quad \partial_t B^i = \partial_t \tilde{\Gamma}^i - \eta B^i. \qquad (2\cdot47)$$

Numerical experiments in 4 dimensions have demonstrated that this set of the gauge conditions together with the BSSN formalism have the required properties. Indeed, this has been used for evolving black hole spacetime (e.g., Ref. 51) for a summary).

In the higher-dimensional spacetime, these conditions may be generalized as

$$\partial_t \alpha - \beta^i \partial_i \alpha = -\eta_\alpha \alpha K, \qquad (2\cdot48)$$

$$\partial_t \beta^i = \frac{(D-1)}{2(D-2)} v_{\text{long}}^2 B^i, \quad \partial_t B^i = \partial_t \tilde{\Gamma}^i - \eta_\beta B^i, \qquad (2\cdot49)$$

where η_α and η_β are constants and v_{long} is the speed of propagation of a gauge mode. In Refs. 37) and 52), the numerical stability was tested using modified

---

[*] This set is often referred to as the moving puncture gauge condition.

dynamical lapse condition $\partial_t \alpha = -\eta_\alpha \alpha K$ and the Γ-driver condition (2·49) with $\sqrt{3}/2 \leq v_{\text{long}} \leq 1$, $1.2 \leq \eta_\alpha \leq 2.0$, and $1/20 r_S \leq \eta_\beta \leq 1/5 r_S$ simulating the Schwarzschild-Tangherlini spacetime, and it turned out that this gauge condition works well also for the higher-dimensional spacetime. However, if the black hole is rapidly rotating, it turned out that the coefficients in this gauge have to be carefully determined for the stable and longterm evolution.[29] This point will be revisited in §3.3.3.

2.4. *Extraction of gravitational-wave flux*

Gravitational waves carry important information for dynamical phenomena. They should be extracted and used for the analysis of numerical results. In 4D numerical relativity, the Newman-Penrose formalism is widely employed for extracting gravitational waves. In higher dimensions, however, such formalism has not been developed yet. To date, two methods have been proposed. One is the gauge-invariant gravitational-wave extraction based on the Kodama-Ishibashi formulation for perturbations of a spherically-symmetric spacetime,[53] and the other is the extraction of energy and angular momentum fluxes employing the Landau-Lifshitz pseudo tensor.[54]

2.4.1. Matching to perturbations of Schwarzschild spacetimes

The method of matching the numerical data with the perturbed spherical spacetime was originally proposed by Abrahams and Evans.[55]–[57] The extension of this method for higher-dimensional numerical relativity was proposed by Witek et al.[45] The basic idea of this approach is that at a distant place of an asymptotically flat spacetime, the spacetime can be regarded as a perturbed Schwarzschild-Tangherlini spacetime, and hence, outgoing gravitational waves can be treated as a perturbation on it using a well-defined formulation for gauge-invariant metric perturbation developed by Kodama and Ishibashi.[53] Here, we briefly summarize the method employed in Ref. 45).

In their formulation of $4 + (D - 4)$ split, Witek et al. assume the $O(D - 3)$ symmetry, where the metric is reduced to the form (2·20), as reviewed in §2.1.3. Suppose $x^\mu (\mu = 0\text{–}3)$ to be (t, x, y, z) and $d\Omega^2_{D-4}$ to be spanned by $\phi^1, ..., \phi^{D-4}$. The spherical-polar coordinates are introduced by

$$x = R \sin\theta \cos\varphi, \quad y = R \sin\theta \sin\varphi, \quad z = R \cos\theta. \qquad (2\cdot50)$$

Here, the relation between the coordinate R and the areal coordinate r has to be specified as a first step. Here, r is related to the area A of the constant radial surface as $r = (A/\Omega_{D-2})^{1/(D-2)}$, where Ω_{D-2} is the $(D - 2)$-dimensional area of a unit sphere. To derive r from the numerical data, some combination of metric components is integrated on the surface $R = \text{const.}$, where the combination is chosen so that the contribution from the first-order perturbation is canceled out after integration. In this manner, one can determine $r(R)$, and then, calculate the perturbative quantities by subtracting the background quantities from the numerical data. Here, the perturbative quantities are separated into three modes according to the Kodama-Ishibashi formulation; the modes with quantum numbers $l = 2, 3, ...$ of the

scalar, vector, and tensor modes. Separation of each mode can be done by (roughly speaking) multiplying each harmonic function to the metric components and integrating on the $r = $ const surface. Then, the master variable Φ_l is calculated for each mode, and finally, the radiated energy for each mode is obtained by integrating the formula for the radiated energy which is written in terms of $\dot{\Phi}_l^2$.

In Refs. 45) and 46), Witek et al. simulated head-on collisions of equal-mass and unequal-mass black holes in 5 dimensions, respectively, where each spacetime has $O(D-2)$ symmetry. There, the gravitational-wave extraction was successfully done using this method. Due to $O(D-2)$ symmetry, gravitational waves include only scalar modes with the quantum numbers $l = 2, 4, ...$ in the equal-mass case and $l = 2, 3, 4, ...$ in the unequal-mass case. This approach has several merits such that one can interpret physical origins of gravitational waves clearly by observing how the radiated energy is distributed to each mode. Also, the energy flux has a definite physical meaning, since the gauge-invariant quantity was used in this study.

2.4.2. Landau-Lifshitz pseudo tensor

Yoshino and Shibata derived the Landau-Lifshitz pseudo tensor[37] in arbitrary dimensions by which energy and angular momentum fluxes of gravitational waves can be extracted. Following Ref. 54), first, a pseudo-tensor is defined by

$$\tilde{g}^{MN} = \sqrt{-g} g^{MN}, \tag{2.51}$$

where g is the determinant of the metric. Then, a super potential is defined by

$$H^{MANB} = \tilde{g}^{MN} \tilde{g}^{AB} - \tilde{g}^{AN} \tilde{g}^{MB}, \tag{2.52}$$

and finally, the Landau-Lifshitz pseudo tensor is by

$$16\pi G t_{\mathrm{LL}}^{MN} = (-g)^{-1} H^{MANB}{}_{,AB} - \left(2R^{MN} - g^{MN} R\right). \tag{2.53}$$

From this definition, the conservation law is derived:

$$\left[(-g)\left(T^{MN} + t_{\mathrm{LL}}^{MN}\right)\right]_{,N} = 0. \tag{2.54}$$

Because the Landau-Lifshitz pseudo tensor is not a tensor, it does not have a covariant meaning in general. However, for a perturbed flat spacetime, the leading-order terms of t_{LL}^{MN} with respect to the perturbative quantities can be used to evaluate the total energy of the system and total radiated energy in a gauge-invariant manner (see below).

In Ref. 54), two expressions for t_{LL}^{MN} are given. The first one is the expression in terms of the Christoffel symbols, which holds for arbitrary dimensionality D. The second one is the expression by the metric functions, which is in D dimensions,

$$16\pi G(-g) t_{\mathrm{LL}}^{MN} = \tilde{g}^{MN}{}_{,A} \tilde{g}^{AB}{}_{,B} - \tilde{g}^{MA}{}_{,A} \tilde{g}^{NB}{}_{,B} + \frac{1}{2} g^{MN} g_{AB} \tilde{g}^{AK}{}_{,L} \tilde{g}^{LB}{}_{,K}$$
$$- \left(g^{MA} g_{BK} \tilde{g}^{NK}{}_{,L} \tilde{g}^{BL}{}_{,A} + g^{NA} g_{BK} \tilde{g}^{MK}{}_{,L} \tilde{g}^{BL}{}_{,A}\right) + g_{AB} g^{KL} \tilde{g}^{MA}{}_{,K} \tilde{g}^{NB}{}_{,L}$$
$$+ \frac{1}{4(D-2)} \left(2 g^{MA} g^{NB} - g^{MN} g^{AB}\right) \left[(D-2) g_{KL} g_{IJ} - g_{LI} g_{KJ}\right] \tilde{g}^{KJ}{}_{,A} \tilde{g}^{LI}{}_{,B}. \tag{2.55}$$

In the following, we consider perturbations on a flat spacetime, for which the metric is written as $g_{MN} = \eta_{MN} + h_{MN}$, and η_{MN} is the flat metric in the Minkowski coordinates. Defining $\hat{h}_{MN} := h_{MN} - (1/2)h\eta_{MN}$, the Landau-Lifshitz pseudo tensor is rewritten to give

$$16\pi G t_{\rm LL}^{MN} = \hat{h}^{MN}{}_{,A}\hat{h}^{AB}{}_{,B} - \hat{h}^{MA}{}_{,A}\hat{h}^{NB}{}_{,B} + \frac{1}{2}\eta^{MN}\hat{h}^{AK}{}_{,L}\hat{h}^{L}{}_{A,K}$$
$$- \left(\hat{h}^{MK}{}_{,L}\hat{h}_K{}^{L,N} + \hat{h}^{NK}{}_{,L}\hat{h}_K{}^{L,M}\right) + \hat{h}^{MA,K}\hat{h}^{N}{}_{A,K} + \frac{1}{2}\hat{h}^{KL,M}\hat{h}_{KL}{}^{,N}$$
$$- \frac{1}{4}\eta^{MN}\hat{h}^{KL,A}\hat{h}_{KL,A} - \frac{1}{4(D-2)}\left(2\hat{h}^{,M}\hat{h}^{,N} - \eta^{MN}\hat{h}^{,A}\hat{h}_{,A}\right), \quad (2\cdot56)$$

where we kept only the second-order quantities of the perturbation.

For the expression (2·56), the conservation law (2·54) for a vacuum spacetime becomes

$$\partial_M t_{\rm LL}^{MN} = 0, \qquad (2\cdot57)$$

where we assume to employ the Minkowski coordinates. This suggests that $t_{\rm LL}^{MN}$ can be interpreted as an effective stress-energy tensor of the gravitational field valid up to second order in h_{MN}. Here, we have to be careful because the Landau-Lifshitz pseudo tensor is not the unique quantity satisfying the condition (2·57) and also because this quantity is not gauge invariant (see Ref. 23)). However, the total radiated energy

$$E_{\rm rad} = \int t^{0i}\hat{n}_i dSdt \qquad (2\cdot58)$$

is gauge-invariant, where dS and $\hat{n}^i$ are the area element and an outward unit normal of a surface at the distant region. Therefore, the Landau-Lifshitz pseudo tensor $t_{\rm LL}^{MN}$ provides a reliable method for evaluating the total radiated energy.

2.5. *Apparent horizon finder*

The apparent horizon is defined as the outermost marginally trapped surface.[23] The trapped surface is defined as a closed $(D-2)$-dimensional surface for which outgoing null geodesic congruences have negative expansion $\theta_+ < 0$. The apparent horizon is defined as the surface of zero expansion $\theta_+ = 0$. Here, the expansion of the outgoing null geodesic congruence is defined by $\theta_+ = \nabla_a k^a$ where k^a is the tangent vector of each null geodesic. The apparent horizon is indispensable in numerical-relativity simulations for finding black hole.[*]

In terms of the geometric quantities on the spacelike hypersurface Σ_t, the equation for zero expansion is written as

$$\theta_+ = D_i s^i - K + K_{ij}s^i s^j = 0, \qquad (2\cdot59)$$

---

[*] Black hole is characterized by the event horizon strictly speaking. However to determine the presence of it, we have to determine the whole spacetime structure. By contrast, the presence or absence of the apparent horizon is determined on each spatial hypersurface Σ_t, and the presence usually implies the presence of the event horizon due to the following theorem: Because of the singularity theorem, the null geodesic congruence of negative expansion eventually plunges into the spacetime singularity, and this implies that the apparent horizon is formed inside of the event horizon assuming the cosmic censorship (see e.g. Ref. 23)).

where s^i denotes the unit normal to the $(D-2)$-dimensional surface of an apparent horizon. To determine the apparent horizon of, e.g., spherical topology, it is common to parameterize the horizon by $r = h(\varphi^i)$, where r is the radial coordinate and φ^i are the appropriately chosen angular coordinates. Rewriting Eq. (2·59) in terms of $h(\varphi^i)$, the equation becomes an elliptic-type equation for $h(\varphi^i)$ with nonlinear source terms composed of h. The resulting equation can be numerically solved using relaxation methods (preparing an initial trial function for the apparent horizon surface and iteratively solving the equation until a convergence is achieved). Although the equation for higher-dimensional cases is slightly different from the equation on the 3D spatial hypersurface Σ_t, it is essentially of the same type, and hence, the numerical scheme for the 4D case can be straightforwardly imported to higher-dimensional cases.

2.6. *Techniques for handling the black hole interior*

In 4D numerical relativity, handling the black hole interior had been an unresolved issue before 2005. However, in 2005, two different prescriptions were developed and this problem was resolved. The first one employs the so-called black hole excision, which was originally proposed by Unruh, together with the GH formalism. The other employs the so-called moving puncture approach together with the BSSN formalism and moving puncture gauge conditions. This enables to simulate black hole spacetimes without excising the interior. These two methods can be extended for higher-dimensional numerical relativity in a straightforward manner.

In the method of black hole excision, one first has to determine the apparent horizon. If the apparent horizon is found, a region inside the apparent horizon is cut out of the computational region, imposing an appropriate boundary condition at the boundary. This method was first developed for a 4D spherical collapse[58] and now it is widely used for simulating not only 4D but also higher-dimensional spacetimes, e.g., for the study of the Gregory-Laflamme instability.[41]

The moving puncture approach can be applied if the BSSN formalism is employed with the moving puncture variables[2] together with the moving puncture gauge conditions. Recently, this has been applied to higher-dimensional problems; head-on collision of equal-mass[38],[45] and unequal-mass[46] black holes in 5 dimensions, grazing collision of two equal mass black holes in 5 and 6 dimensions,[59] and evolution of rapidly rotating black holes in 5–8 dimensions.[28],[29]

2.7. *Adaptive mesh refinement*

The adaptive mesh refinement (AMR) algorithm (or the nested grid algorithm) is a prescription that enables to simulate a system of a large dynamical range with a relatively inexpensive computational cost. In this approach, several refinement levels with different grid spacing and computational domain size are prepared. In the neighborhood near the compact objects such as a black hole, the fine refinement levels with small grid size are assigned, while far from the compact objects, coarser levels are assigned. Gravitational waves have to be extracted in the wave zone. For the extraction, we prepare a coarse refinement level with large domain size to cover a local wave zone (however, its grid size has to be at least by one order of magnitude

smaller than the wavelength of gravitational waves).

The AMR algorithm is widely employed in 4D numerical relativity, e.g., in the simulations of high-velocity collisions of black holes.[60)–62)] In such simulations, finer levels are assigned in the vicinity of moving black holes and relatively coarser levels are assigned for the distant region. The AMR algorithm can be straightforwardly imported to the higher-dimensional cases.

Here, we point out that the AMR algorithm has been playing an important role in higher-dimensional numerical relativity. For example, for the study of the Gregory-Laflamme instability,[41)] some part of the black string becomes more and more narrow; Lehner and Pretorius show that it seems to continue until the radius of the string reaches zero. To avoid losing the accuracy in such a simulation, one has to continuously increase the resolution around the narrow string. For such purpose, the AMR algorithm is indispensable. The AMR algorithm was also important in the simulations of rapidly rotating Myers-Perry (MP) black holes,[28), 29)] because the throat of a rapidly rotating MP black hole is very long, and thus, the variables steeply varies in the neighborhood of the horizon.

2.8. *Initial data preparation*

As mentioned in §2.1.2, the initial data has to satisfy the Hamiltonian and the momentum constraints (see Eqs. (2·4) and (2·5)). Here, we review a formulation for preparing the puncture-type initial data in higher dimensions.[63), 64)] This may be regarded as an extension of the well-known formulations by Brill and Lindquist,[65)] Bowen and York,[66)] and Brandt and Brügmann.[67)] The initial condition in this formulation is employed for a simulation of head-on collision of two black holes,[38), 45), 46)] which will be reviewed in §3.2. Methods for preparing initial data for the study of the Gregory-Laflamme instability and of the Myers-Perry black holes will be reviewed separately in §§3.1 and 3.3.

In the Bowen-York approach, the initial spatial hypersurface is assumed to be conformally flat

$$h_{ij} = \Psi^{4/(D-3)}\delta_{ij}, \tag{2·60}$$

and to be maximally sliced, $K = 0$. Here, the Cartesian coordinates x^i are employed. For convenience, a weighted extrinsic curvature is defined by $\widehat{K}_{ij} = \Psi^2 K_{ij}$. Here, the index of $\widehat{K}_{ij}$ is raised and lowered by δ_{ij} (i.e., $\widehat{K}^i_j = \Psi^{2(D-1)/(D-3)}K^i_j$ and $\widehat{K}^{ij} = \Psi^{2(D+1)/(D-3)}K^{ij}$). Then the Hamiltonian and momentum constraints become

$$\nabla_{\text{f}}^2 \Psi = -\frac{D-3}{4(D-2)}\widehat{K}_{ij}\widehat{K}^{ij}\Psi^{-(3D-5)/(D-3)}, \tag{2·61}$$

$$\partial^i \widehat{K}_{ij} = 0, \tag{2·62}$$

where $\partial_i(= \delta_{ij}\partial^j = \partial^i)$ denotes the ordinary derivative with respect to the Cartesian coordinates (x^i) and $\nabla_{\text{f}}^2 := \partial^i \partial_i$. Following Bowen and York,[66)] we assume that $\widehat{K}_{ij}$ takes the following form

$$\widehat{K}_{ij} = \partial_i W_j + \partial_j W_i - \frac{2}{N}\delta_{ij}\partial_k W^k, \tag{2·63}$$

where $N = D - 1$. We further decompose W_i as

$$W_i = \frac{3D - 5}{D - 3} B_i - \left(\partial_i \chi + x^j \partial_i B_j \right), \tag{2.64}$$

with auxiliary functions B_i and χ. Then Eq. (2.62) becomes

$$0 = \frac{3D - 5}{D - 3} \nabla_f^2 B_i - \frac{2(D - 2)}{D - 1} \partial_i \nabla_f^2 \chi - x^j \partial_i \nabla_f^2 B_j - \frac{D - 3}{D - 1} \partial_i \left(x^j \nabla_f^2 B_j \right). \tag{2.65}$$

Hence the momentum constraint is satisfied if

$$\nabla_f^2 B_i = 0 \quad \text{and} \quad \nabla_f^2 \chi = 0 \tag{2.66}$$

are satisfied. To give linear momenta to black holes, one can choose

$$B_i = -\frac{2\pi G P_i}{(D - 2)\Omega_{D-2} R^{D-3}} \quad \text{and} \quad \chi = 0, \tag{2.67}$$

where P_i is a constant vector, Ω_{D-2} the $(D - 2)$-dimensional area of a unit sphere, and $R = |x^i|$. Then,

$$\widehat{K}_{ij} = \frac{4\pi(D - 1)G}{(D - 2)\Omega_{D-2} R^{D-2}} \left\{ P_i n_j + P_j n_i + P_k n^k \left[(D - 3) n_i n_j - \delta_{ij} \right] \right\}, \tag{2.68}$$

where $n^i = x^i / R$. This solution provides the extrinsic curvature for one boosted black hole located at $R = 0$, and P_i agrees with the ADM momentum

$$P_i = \frac{1}{8\pi G} \int_{R \to \infty} \left(K_{ij} n^j - K n_i \right) dS. \tag{2.69}$$

Since the momentum constraint (2.62) is a linear equation, we can superpose arbitrary number of black holes. Denoting the locations of n black holes by $x_a^i (a = 1, ..., n)$, the solution of the extrinsic curvature is written as

$$\widehat{K}_{ij} = \sum_{a=1}^{n} \frac{4\pi(D - 1)G}{(D - 2)\Omega_{D-2} R_a^{D-2}} \Big\{ (P_a)_i (n_a)_j + (P_a)_i (n_a)_j$$
$$+ (P_a)_k (n_a)^k \left[(D - 3)(n_a)_i (n_a)_j - \delta_{ij} \right] \Big\}, \tag{2.70}$$

where $R_a = |x^i - x_a^i|$, $n_a^i = (x^i - x_a^i)/R_a$, and $(P_a)_i$ denotes the momentum of the a-th black hole.

The conformal factor Ψ is determined by solving the Hamiltonian constraint (2.61). Following Brandt and Brügmann,[67] Ψ is assumed to have the following form

$$\Psi = \Psi_{\text{BL}} + \psi, \tag{2.71}$$

where

$$\Psi_{\text{BL}} \equiv 1 + \frac{4\pi G}{(D - 2)\Omega_{D-2}} \sum_{a=1}^{n} \frac{M_a}{R_a^{D-3}}, \tag{2.72}$$

and M_a denotes the mass parameter of a-th black hole. Then, the equation for ψ becomes

$$\nabla_{\mathrm{f}}^2 \psi = -\frac{(D-3)}{4(D-2)} \widehat{K}_{ij} \widehat{K}^{ij} (\Psi_{\mathrm{BL}} + \psi)^{-(3D-5)/(D-3)}. \tag{2.73}$$

The solution in this procedure provides the so-called "puncture" space with n Einstein-Rosen bridges and $n+1$ asymptotically flat regions (say, one upper sheet and n lower sheets). Since the right-hand side of Eq. (2.73) behaves like $O(R_a^{D-3})$ for $R_a \to 0$, a regular solution for ψ can be obtained numerically as in the 4D case.[67] The ADM mass M_{ADM} is given by

$$M_{\mathrm{ADM}} = -\frac{(D-2)}{4\pi(D-3)G} \int_{R\to\infty} \partial_i \Psi n^i dS$$

$$= \sum_{a=1}^{n} M_a + \frac{1}{16\pi G} \int_{\Sigma} \widehat{K}^{ij} \widehat{K}_{ij} \Psi^{-(3D-5)/(D-3)} d^{D-1}x, \tag{2.74}$$

where the Gauss law is used in the second line. The numerical solution of Ψ for head-on collision of two equal-mass black holes is found in Ref. 64).

2.9. (Semi)analytic solutions for benchmark tests

To confirm the reliability of a code newly developed, benchmark tests are necessary. One of the standard tests is to check the convergence of numerical results with different grid resolutions: If the numerical solution shows a convergence property that is expected in the adopted scheme, we can believe its reliability. Another method is to simulate a spacetime for which analytic (or semi-analytic) solution is known and to compare the numerical results with it. Here, we summarize the analytic solutions that are useful for the benchmark tests.

2.9.1. Geodesic slice of Schwarzschild-Tangherlini spacetime

First, we show an analytic solution of the 5D spherical black hole in the geodesic slicing. The well-known metric form of the higher-dimensional black hole (the so-called Schwarzschild-Tangherlini metric) is

$$ds^2 = -f(r)dt^2 + \frac{dr^2}{f(r)} + r^2 d\Omega_3^2, \qquad f(r) = 1 - \frac{r_S^2}{r^2}, \tag{2.75}$$

where $d\Omega_3^2$ is the line element of a 3D unit sphere and r_S is the Schwarzschild-Tangherlini radius $r_S = \sqrt{8GM/3\pi}$. Because the coordinates in this metric are not well-behaved inside the event horizon, the metric of this spacetime is rewritten in terms of the Gaussian normal coordinates starting from the $t = 0$ hypersurface as

$$ds^2 = -d\tau^2 + \frac{\left[r_0^2 + (r_S/r_0)^2\tau^2\right]^2}{\left[r_0^2 - (r_S/r_0)^2\tau^2\right]} \frac{dR^2}{R^2} + \left[r_0^2 - (r_S/r_0)^2 \tau^2\right] d\Omega_3^2, \tag{2.76}$$

where r_0 is defined by
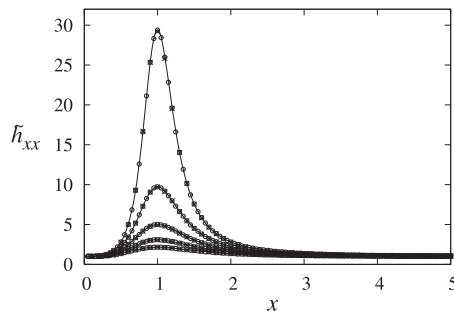
$$r_0 = R\left(1 + \frac{r_S^2}{4R^2}\right). \tag{2.77}$$

Fig. 1.   Snapshots of $\tilde{h}_{xx}$ along the x-axis for $\tau/r_S = 0.5$, 0.6, 0.7, 0.8, and 0.9. The unit of x is $r_S/2$. The grid resolutions are $\Delta x = 0.1$ ($\times$) and 0.05 ($\odot$). The solid curves denote the analytic solutions. The figure is taken from Ref. 37).

The meaning of these coordinates is explained as follows. Consider a geodesic congruence of test particles that are initially at rest. Then, each geodesic labels the radial coordinate and its proper time is equal to the time coordinate. At $\tau = 0$, the spatial slice agrees with the Einstein-Rosen bridge written with the isotropic radial coordinate R (compare r_0 with the conformal factor for $P_i = 0$ and $n = 1$ of Eqs. (2·71) and (2·72)). This is analogous to the Novikov coordinates in the 4D Schwarzschild spacetime.[68),69)] This line element shows that the RR component of the metric diverges at $\tau = r_0^2/r_S$, and this occurs when the slice hits the singularity.

In the line element (2·76), τ and R are always time and radial coordinate, and thus, this coordinate system can be employed in numerical relativity for a benchmark test. In this test, a simulation is done with the gauge conditions $\alpha = 1$ and $\beta^i = 0$, until the computation crashes approximately at the crash time $\tau_{\text{crash}} = r_S$. Figure 1 shows a comparison between the analytic solution (solid curves) and the data obtained by Yoshino's code[37)] with grid size $\Delta x/r_S = 0.1$ (crosses, $\times$) and 0.05 (circles, $\odot$). Here, the snapshots of xx component of the conformal 4D metric $\tilde{h}_{xx}$ along the x-axis are drawn for $\tau/r_S = 0.5$, 0.6, 0.7, 0.8, and 0.9. This shows that the values of $\tilde{h}_{xx}$ rapidly increase and blow up around $x = 1$, and agree approximately with the analytic solutions (2·76) (solid curves). It is also checked that the deviation of numerical solution from the analytic one shows the 4th-order convergence in a code implementing a 4th-order finite differencing.[37)]

2.9.2.   Limit surface of Schwarzschild-Tangherlini spacetime

As the second analytic solution, we describe the limit surface of maximally sliced evolution (i.e. evolution keeping $K = 0$) of a Schwarzschild-Tangherlini spacetime. In the 4D Schwarzschild black hole, it was shown that the sequence of the maximal slices never hits the curvature singularity but asymptotes to the so-called limit surface,[70)] and the analytical expression of the limit surface was given in Ref. 71). The limit surface provides a useful test for calibrating numerical-relativity codes. Namely, if we adopt the limit surface as the initial data, the spacelike hypersurface has to be unchanged during the time evolution under certain gauge conditions.

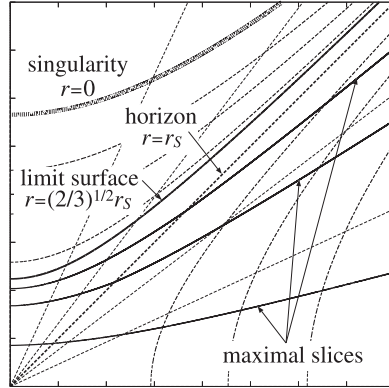This study was extended to higher dimensions by Nakao et al.[52)] Figure 2 shows

Fig. 2. The sequence of maximal slicing surfaces in the Kruskal diagram of Schwarzschild-Tangherlini spacetime with $D = 5$. The dotted curves show the $r = $ const. The limit surface is given by $r = \sqrt{2/3}r_S$. The figure is taken from Ref. 52).

the Kruskal diagram of the 5D Schwarzschild-Tangherlini spacetime. The sequence of maximal-sliced hypersurfaces (starting from the time-symmetric slice) is shown by the solid curves. The sequence asymptotes to $r = \sqrt{2/3}r_S$, which is the limit surface, and the formula for the limit surface can be given analytically also in the 5D case. The limit surface turns out to be conformally flat, and thus, we can introduce the spherical-polar coordinates (R, ϕ_i) in the flat space. The relation between R and the Schwarzschild radial coordinate r is

$$R = \frac{r}{6}\left(3 + \sqrt{3\left[(r_S/r)^2 + 3\right]}\right)\left(\frac{(5 + 2\sqrt{6})\left[3 - 2(r_S/r)^2\right]}{2(r_S/r)^2 + 15 + 6\sqrt{2\left[(r_S/r)^2 + 3\right]}}\right)^{1/\sqrt{6}}. \quad (2\cdot78)$$

In terms of the BSSN variables,

$$\chi = \left(\frac{R}{r}\right)^2, \quad \alpha = \sqrt{1 - \left(\frac{r_S}{R}\right)^2\chi + \frac{4}{27}\left(\frac{r_S}{R}\right)^6\chi^3}, \quad (2\cdot79)$$

$$\beta^R = \frac{2}{3\sqrt{3}}\chi^2\left(\frac{r_S}{R}\right)^3, \quad \tilde{A}^R_{\ R} = -3\tilde{A}^{\phi_i}_{\ \phi_i} = -\frac{2}{\sqrt{3}}\chi^2\frac{r_S^3}{R^4}. \quad (2\cdot80)$$

Here, r has to be written as a function of R numerically, and then, the nontrivial components can be calculated.

Figure 3 shows the values of α, β^x, $\tilde{A}_{yy}$, and χ along the x axis at a selected time slice. Adopting the data shown by the solid curves as the initial condition, Yoshino[37] evolved this spacetime using the dynamical gauge condition and Γ-driver condition. The data at $t = 50r_S$ (after the time evolution) are plotted by the circles. It is confirmed that all the BSSN variables are approximately unchanged in time. In this manner, we can check the accuracy of the code using the limit surface.

2.9.3. Linear gravitational waves

The third one is the semi-analytic solution of gravitational waves on a 5D flat spacetime.[37] Here, we denote the metric perturbation as δg_{ab}, which obeys linearized
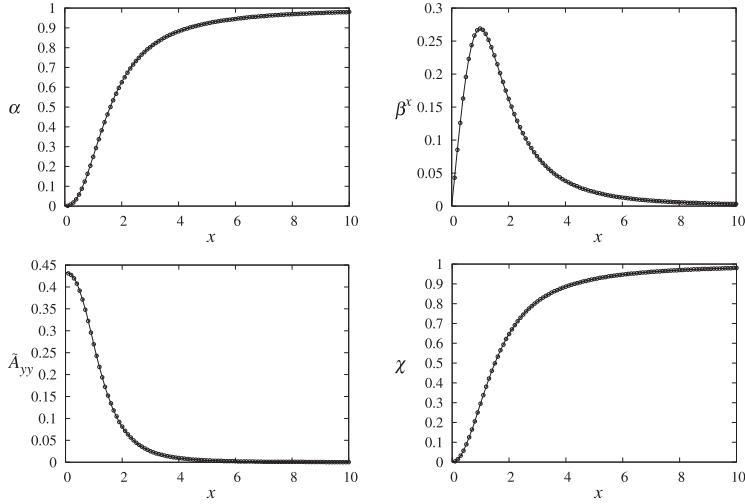
Fig. 3. The analytic solutions of α, β^x, $\tilde{A}_{yy}$, and χ along the x-axis for the limit surface of the 5D spherical black hole (solid curves), and the numerical data after the time evolution at $t = 50r_S$ ($\odot$). Here, the unit of the length is $r_S/2$. The data remains approximately stationary in the time evolution. The figure is taken from Ref. 37).

Einstein's equation. Adopting the gauge conditions, $\alpha = 1$ and $\beta^i = 0$ (i.e. $\delta g_{00} = \delta g_{0i} = 0$), the spatial components of linearized Einstein's equation become

$$\delta \ddot{g}_{ij} = \Delta(\delta g_{ij}), \tag{2.81}$$

where Δ is the flat 4D Laplacian.

We then use the formulation for perturbations of higher-dimensional Schwarzschild black holes of Ref. 53) with zero black-hole mass. Namely, the perturbation is decomposed into the scalar, vector, and tensor modes (with respect to the 3D unit sphere) using spherical harmonic functions, and the master equations are derived for the gauge-invariant variables. Here, the method for the spherical harmonic expansion should be adopted but the master equations are not because we are interested in explicit special solutions under a fixed gauge in numerical relativity.

Here, we focus on the tensor mode as an example. Perturbation δg_{ij} of the tensor type is expanded in terms of the harmonic tensors $\mathbb{T}_{IJ}$ satisfying

$$[\hat{\Delta}_3 + l(l+2) - 2]\mathbb{T}_{IJ} = 0, \tag{2.82}$$

$$\mathbb{T}^I{}_I = 0, \qquad \hat{D}_J \mathbb{T}^J{}_I = 0, \tag{2.83}$$

and the perturbation is given in the form

$$\delta g_{ij} = \begin{pmatrix} 0 & 0 \\ * & rh(t,r)\mathbb{T}_{IJ} \end{pmatrix}. \tag{2.84}$$

If we impose, e.g., the $U(1) \times U(1)$ symmetry to the space, the harmonic tensors for

$l = 2$ are

$$\mathbb{T}_{IJ} = \begin{pmatrix} A & 0 & 0 \\ * & A\sin^2\theta(1 - 3\sin^2\theta) & B\sin^2\theta\cos^2\theta \\ * & * & A\cos^2\theta(3\sin^2\theta - 2) \end{pmatrix}, \qquad (2\cdot85)$$

where A and B are arbitrary constants, and the (θ, φ, ψ) coordinates are introduced as

$$\begin{aligned} x &= r\sin\theta\cos\varphi, \quad y = r\sin\theta\sin\varphi, \\ z &= r\cos\theta\cos\psi, \quad w = r\cos\theta\sin\psi. \end{aligned} \qquad (2\cdot86)$$

From Eq. (2·81), the equation for h becomes

$$\ddot{h} = h_{,rr} + \frac{1}{r}h_{,r} - \frac{9}{r^2}h, \qquad (2\cdot87)$$

and a special solution can be written as

$$h = \mathrm{Re}\left[\int d\omega f(\omega)e^{i\omega t}J_3(\omega r)\right], \qquad (2\cdot88)$$

where $f(\omega)$ is an arbitrary function of ω, and J_3 is the Bessel function of third order,

$$J_3(z) = \frac{1}{2\pi}\int_0^{2\pi} d\vartheta\cos(3\vartheta - z\sin\vartheta). \qquad (2\cdot89)$$

To constitute a solution for the propagation of a gravitational-wave packet, we set $f(\omega) = -i\sqrt{2\pi}A_0e^{-\omega^2/2\omega_0^2}$. Then, Eq. (2·88) is integrated to give

$$h(t, r) = A_0\omega_0\int_0^{2\pi} d\vartheta\sin(3\vartheta)e^{-\omega_0^2(t - r\sin\vartheta)^2/2}. \qquad (2\cdot90)$$

The numerical integration in this formula can be computed easily. In this solution, $h(0, r) = 0$ (and thus $\delta g_{ij} = 0$), whereas $\dot{h}(0, r) \neq 0$ (and thus $\delta\dot{g}_{ij} \neq 0$).

We note that in a similar manner, the semi-analytic solutions of gravitational-wave packet can be obtained also for scalar and vector modes.[37]

2.9.4. *Close-slow collision of two black holes*

Finally, semi-analytic solutions of gravitational waves emitted in the head-on collision of two Bowen-York-type black holes in the close-slow limit is described.[63],[64] The close-limit approximation was first studied by Price and Pullin[72] in the 4D case, and its solutions have been used for calibrating the results in numerical relativity. The idea of this approximation comes from the fact that if the separation between two black holes is small enough, a common event horizon should be formed to enclose two black holes, and the geometry outside the event horizon may be approximated by a perturbed Schwarzschild black hole. Then, the time evolution of the system may be approximately determined by the linear perturbation equations for which numerical integration is performed much more easily than in the numerical-relativity simulation. Here, we review a higher-dimension version on this study.

In §2.8, we explained a higher-dimensional generalization of the Brandt-Brügmann formalism for preparing initial data. Using this method, we can construct initial data of two moving black holes located at $z = \pm z_0$ along the z-axis. Here, the spatial coordinates chosen are $(x_1, ..., x_{D-2}, z)$, and we denote the momenta of two black holes by $P^{(\pm)i} = (0, ..., 0, \mp P)$. In the close-slow approximation, we should assume that $z_0 \ll r_S(M_0)$, $P \ll M_0$, and $z_0/r_S(M_0) \sim P/M_0$, and evaluate gravitational-wave energy up to order of $(z_0/r_S(M_0))^2$. In the following, the gravitational radius of the system $r_S(M_0)$ is used as the unit of the length (i.e., $r_S(M_0) = 1$). In the spherical polar coordinates, the extrinsic curvature $K_{ij} = K_{ij}^{(+)} + K_{ij}^{(-)}$ is calculated to give

$$\widehat{K}_R^R = (z_0 P/M_0) \frac{D-1}{2} \left[D - 4 - D(D-3) \cos^2\theta \right] R^{-(D-1)} + O(z_0^2 P/M_0), \quad (2\cdot 91)$$

$$\widehat{K}_\theta^\theta = (z_0 P/M_0) \frac{D-1}{2} \left[(D-3) \cos^2\theta + 1 \right] R^{-(D-1)} + O(z_0^2 P/M_0), \quad (2\cdot 92)$$

$$\widehat{K}_{\phi_*}^{\phi_*} = (z_0 P/M_0) \frac{D-1}{2} \left[(D-1) \cos^2\theta - 1 \right] R^{-(D-1)} + O(z_0^2 P/M_0), \quad (2\cdot 93)$$

and $\widehat{K}_{R\theta} = O(z_0^3 P/M_0)$ in the close limit $z_0 \ll 1$. The leading-order term of $\widehat{K}_{ab}$ is found to be of $O(z_0 P/M_0)$ and hence the right-hand side of the Hamiltonian constraint (2·61) is of $O(z_0^2 P^2/M_0^2)$. In the close-slow approximation adopted here, such terms are higher order and ignored. Thus, $\psi = 0$ and $M_{\mathrm{ADM}} = M_0$ in this approximation. As a result, the conformal factor is given by the Brill-Lindquist one

$$\Psi \simeq \Psi_{\mathrm{BL}} = 1 + \frac{1}{8} \left(\frac{1}{R_+^{D-3}} + \frac{1}{R_-^{D-3}} \right), \quad (2\cdot 94)$$

where $R_\pm := \sqrt{\sum_i (x^i)^2 + z^2}$. By transforming from the isotropic coordinate to the Schwarzschild-like coordinate

$$r = R\Psi_0^{2/(D-3)}, \quad \Psi_0 = 1 + \frac{1}{4R^{D-3}}, \quad (2\cdot 95)$$

we find that the system is regarded as a perturbed Schwarzschild black hole

$$ds^2 \simeq \left(\frac{\Psi_{\mathrm{BL}}}{\Psi_0} \right)^{4/(D-3)} \left[\frac{dr^2}{f(r)} + r^2 (d\theta^2 + \sin^2\theta d\Omega_{D-3}^2) \right], \quad f(r) = 1 - \frac{1}{r^{D-3}}, \quad (2\cdot 96)$$

$$\left(\frac{\Psi_{\mathrm{BL}}}{\Psi_0} \right)^{4/(D-3)} = 1 + \frac{1/(D-3)R^{D-3}}{1 + 1/4R^{D-3}} \left(\frac{z_0}{R} \right)^2 C_2^{[(D-3)/2]}(\cos\theta) + O(z_0^4), \quad (2\cdot 97)$$

where $C_\ell^{[\lambda]}$ denotes the Gegenbauer polynomials defined by the generating function

$$(1 - 2xt + t^2)^{-\lambda} = \sum_{\ell=0}^{\infty} C_\ell^{[\lambda]}(x) t^\ell. \quad (2\cdot 98)$$

This initial data is evolved using a perturbation method in the Schwarzschild space-time. From Eqs. (2·91)–(2·93), (2·96), and (2·97), it is found that the leading order of the perturbation contains only the $\ell = 2$ mode.

The gauge-invariant method for the perturbation around the spherical black hole was developed by Kodama and Ishibashi.[53)] They derived a master equation for a variable Φ, which is related to the gauge-invariant quantities of the perturbation, as

$$\frac{\partial^2 \Phi}{\partial t^2} - \frac{\partial^2 \Phi}{\partial r_*^2} + V_S \Phi = 0, \tag{2.99}$$

where

$$V_S(r) = \frac{f(r)Q(r)}{16r^2 H^2(r)}, \tag{2.100}$$

and

$$H(r) = m + (1/2)(D-1)(D-2)x, \quad x = 1/r^{D-3}, \tag{2.101}$$

$$m = k^2 - D + 2, \quad k^2 = \ell(\ell + D - 3), \tag{2.102}$$

$$\begin{aligned}
Q(r) = &(D-2)^4(D-1)^2 x^3 \\
&+ (D-2)(D-1)\left[4(2D^2 - 11D + 18)m + (D-1)(D-2)(D-4)(D-6)\right]x^2 \\
&- 12(D-2)\left[(D-6)m + (D-1)(D-2)(D-4)\right]mx \\
&+ 16m^3 + 4D(D-2)m^2.
\end{aligned} \tag{2.103}$$

r_* denotes the tortoise coordinate defined by $r_* = \int dr/f(r)$. Initial values of Φ and $\dot{\Phi}$ (a dot denotes the time derivative hereafter) are related to the metric perturbation and $\widehat{K}_{ab}$, respectively, as

$$\Phi(0,r) = (z_0^2)\frac{(D-2)\sqrt{r}\left[D^2 - D + 2 + (D-2)(D+1)\sqrt{f}\right]}{4(D-1)(D-3)K_2^{[D-2]}H(r)R^{(D+1)/2}}, \tag{2.104}$$

$$\dot{\Phi}(0,r) = -(z_0 P/M_0)\frac{2(D-2)\sqrt{f}[2D + (D-1)x]}{(D-3)K_2^{[D-2]}r^{D/2}[2D + (D-1)(D-2)x]}, \tag{2.105}$$

where the definition of $K_2^{[D-2]}$ is given in Refs. 63) and 73). Since Eq. (2.99) is a linear equation, Φ is naturally decomposed into two parts

$$\Phi = (z_0^2)\widehat{\Phi}_{\mathrm{BL}} + (z_0 P/M_0)\widehat{\Phi}_{\mathrm{BY}}. \tag{2.106}$$

The numerical solutions of $\widehat{\Phi}_{\mathrm{BL}}$ and $\widehat{\Phi}_{\mathrm{BY}}$ can be found in Refs. 63) and 64), respectively. The total radiated energy of gravitational waves is calculated by the formula (see Refs. 63) and 73) for a derivation)

$$E_{\mathrm{rad}} = \frac{k^2(D-3)(k^2 - D + 2)}{32(D-2)\pi G}\int \dot{\Phi}^2 dt. \tag{2.107}$$

Substituting Eq. (2.106) into the above formula, E_{rad} is rewritten as

$$\frac{E_{\mathrm{rad}}}{M_0} = c_1 z_0^4 + c_2 z_0^3 (P/M_0) + c_3 z_0^2 (P/M_0)^2, \tag{2.108}$$

where c_1, c_2, and c_3 are constants determined by numerical integration. These values are listed in Table I. The formula (2.108) together with Table I may be used for calibrating the results derived by the fully nonlinear simulation in higher-dimensional numerical relativity.

Table I.   The values of c_1, c_2 and c_3 of Eq. (2·108) for $D = 4$–11.

D	4	5	6	7	8	9	10	11
c_1	0.0252	0.0245	0.0290	0.0288	0.0258	0.0223	0.0194	0.0172
c_2	-0.165	-0.243	-0.294	-0.287	-0.251	-0.213	-0.182	-0.158
c_3	0.343	0.671	0.808	0.765	0.647	0.539	0.456	0.396

§3.   Simulations

In this section, several simulations of higher-dimensional numerical relativity performed to date are reviewed. We in particular pick up three topics, numerical study of the Gregory-Laflamme instability for a black string,[41] black hole collisions,[38), 45), 46), 60)–62)] and numerical study of the bar-mode instability for rapidly rotating Myers-Perry (MP) black holes with one rotational parameter.[28), 29)] Although we do not review in detail here, we also refer the readers to the study by Sorkin[42] on development of an axisymmetric $(2 + 1$-dimensional) code for D-dimensional spacetimes using the GH formalism and its application to complex scalar fields minimally coupled to gravity in Kaluza-Klein spacetimes for $D = 5$ and 6.

3.1.   *Gregory-Laflamme instability of black string*

The 5D black string is one of the simplest solutions of the black objects in 5D general relativity. The metric of this solution is written as

$$ds^2 = -f(r)dt^2 + \frac{dr^2}{f(r)} + r^2 d\Omega_2^2 + dz^2, \qquad f(r) = 1 - \frac{2G_N M}{r}, \qquad (3·1)$$

where G_N is a 4D gravitational constant that is related to the 5D one as $G = G_N L$ if the z direction is compactified with the scale L. The black string is shown to be unstable against long wavelength deformation along the z direction (see also Chapter 6 of this supplement). There is a critical wavelength L_c for the instability; if the wavelength of a perturbation is longer than L_c, the instability sets in. The value of L_c are evaluated numerically, and L_c is of order $4\pi G_N M$. This implies that the black string is unstable if the compactification scale is longer than $L > L_c$. The end state of the Gregory-Laflamme instability has been inferred by many works. Among them, Horowitz and Maeda[74] gave a proof for the fact that the horizon cannot pinch off in a finite affine-parameter time under very weak assumptions, and conjectured the presence of a new stable state that is not translationally invariant in the z direction.

To find the final fate of the Gregory-Laflamme instability, numerical-relativity simulation is probably the unique approach. A pioneer work was done by Choptuik et al.[13] Their simulation was performed assuming the spherical symmetry for the 3D space composed of (r, θ, φ), and adding a perturbation along the z axis. An excision algorithm was employed to handle the interior of the black-string horizon. The lapse function and shift vector were chosen to be $\alpha = \alpha_{\rm BS}$, $\beta^z = 0$, and $\beta^r = 2\alpha K_{\theta\theta}/h_{\theta\theta,r}$, where $\alpha_{\rm BS}$ is the lapse of the static black string in the Eddington-Finkelstein coordinates. The initial data was calculated by giving the distortion in
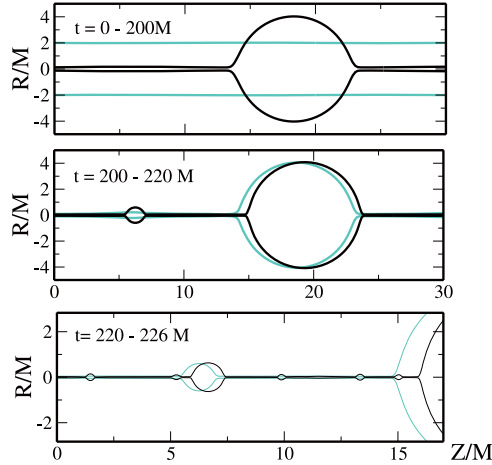
Fig. 4. Snapshots of the apparent horizon of a black string for $t/G_N M = 0$, 200 (above), 200, 220 (middle) and 220, 226 (below). The formation of first-, second-, and third-generation black-hole satellites is seen. The figure is taken from Ref. 41).

the z direction as

$$g_{\theta\theta}(0, r, z) = 1 + A \sin\left(z\frac{2\pi q}{L}\right) e^{-(r-r_0)^2/\delta_r^2}, \qquad (3\cdot2)$$

and solving the Hamiltonian and momentum constraints to give the other metric components and extrinsic curvatures. The simulation was performed for $L = 1.4L_c$. Although the system was successfully evolved, a new stable state was not reached until the end of the simulation at $t = 164G_N M$. The authors showed the embedding diagram of the apparent horizon (see Fig. 4 of Ref. 13)), and the resulting configuration looks like large spherical black holes connected by thin black strings. However the end state was still evolving in time. In Ref. 14), the behavior of null geodesic congruence (which approximately denotes the event horizon) was studied in detail, and it was found that the affine-parameter time becomes very large at the end of the simulation. The authors discussed the possibility that the horizon may pinch off in the infinite affine-parameter time.

In a recent paper, the most successful simulation to date was reported by Lehner and Pretorius.[41] In this simulation, the authors used a 4th-order accurate new code for which GH formalism (§2.1.1) and modified version of the cartoon method (§2.2.2) together with the AMR (§2.7) and black hole excision (§2.6) algorithms were employed. The simulation was performed for $L = 20G_N M \simeq 1.4L_c$ with the outer boundary located at $320G_N M$. The initial data was prepared in the same manner as in Ref. 13). Figure 4 shows the snapshots of an embedding diagram of the apparent horizon reported in Ref. 41). Up to $t = 200G_N M$, the results are similar to those of the previous simulation.[13] However, after $t = 220G_N M$, some part of the thin string segment continuously generates a small black-hole-like object while other parts continue to shrink to be a thinner string. The authors call the black-hole-like objects "satellites". As the time goes further ($t = 226G_N M$), new smaller satellites are formed while other parts continue to shrink. The satellite black holes are formed

in a self-similar cascade way, and this suggests the scenario of horizon pinch off in an infinite affine-parameter time.

The important question here is whether the singularity is visible from observers located outside, and this question is closely related to whether the infinite affine-parameter time corresponds to an infinite or a finite asymptotic time. Here, the asymptotic time implies the time coordinate that penetrates the horizon and is reduced to the Minkowski time at spacelike infinity. The harmonic time coordinate employed in the simulation is an example of such coordinate. In the case of an infinite asymptotic time, the horizon shrinks more and more slowly in the asymptotic time as well as in the affine parameter, and the observers located outside the horizon cannot see the horizon pinch off. In the case of a finite asymptotic time, the singularity formed in the horizon pinch-off would be able to affect the distant region, and thus, the naked singularity is formed and the cosmic censorship is violated. The authors discussed the latter possibility. The reason is that the time scale for the formation of the next-generation satellite/string-segments is proportional to the local string radius, and becomes shorter and shorter as the generation is increased. This suggests that the string radius reaches zero in the finite asymptotic time as a result of self-similar cascade. This indicates that the cosmic censorship may be generically violated in 5D general relativity.

3.2. *Black hole collisions and scatterings*

Now we turn our attention to the simulations of black hole collisions performed to date. First, we review the simulations of head-on collisions of black holes in higher dimensions, and then, those of high-velocity collisions of black holes in 4 dimensions are summarized.

3.2.1. Black hole head-on collision in $D = 5$

The simulations for head-on collisions of two black holes in 5 dimensions were first reported by Zilhao et al.,[38] and subsequently detailed analyses were reported by Witek et al.[45] They adopted the so-called Brill-Lindquist initial data for two equal-mass black holes as the initial condition (see §2.9.4). The simulation was done in a (x, y, z)-plane, where z-axis is the axis of the $O(3)$ symmetry, and the initial positions of two punctures are $z = \pm z_0$ on the z axis. The spacetime was evolved using the code for which the $4 + (D - 4)$ splitting method is implemented.

The left panel of Fig. 5 shows the snapshots of the conformal factor χ on the z axis for $t/r_S(M) = 0$, 5, 20, 40, and 256 reported in Ref. 38). As in the 4D simulations, the positions of the punctures, at which $\chi = 0$, approach each other and eventually merge. In Ref. 45), the coordinate time t_{CAH}, at which the common apparent horizon is formed, was evaluated as a function of initial separation L (which is defined by the proper distance along the z axis between the two apparent horizons), and it was found that t_{CAH} agrees remarkably well with the free-fall time in Newtonian gravity, $t_{free-fall} = (L/r_S)^2 r_S$. The right panel of Fig. 5 shows the gravitational waveforms for the $l = 2$ scalar mode extracted by the method reported in Ref. 45) (reviewed in §2.4.1). This shows it possible to follow the evolution from the initial burst to the ringdown phase. The total radiated energy is estimated as
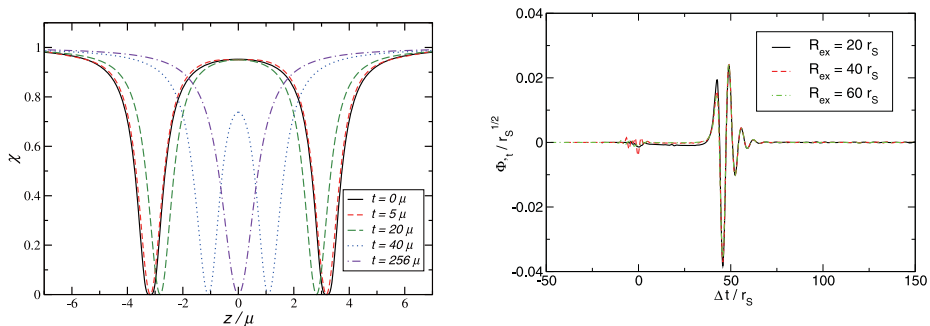
Fig. 5. Left panel: Snapshots of the conformal factor χ for $t/r_S(M) = 0$, 5, 20, 40 and 256 in the head-on collision of two equal-mass black holes initially at rest. Right panel: The gravitational waveform for the $l = 2$ scalar mode extracted by matching with perturbation of a Schwarzschild-Tangherlini black hole. The results with three extract positions $R_{\rm ex}/r_S = 20$, 40, and 60 are shown. The figure is taken from Ref. 45).

$E_{\rm rad}/M \simeq (8.9 \pm 0.6) \times 10^{-4}$, which agrees well with the estimate from the variation of the total area of the apparent horizons.

In a recent paper,[46] the authors performed a head-on collision of unequal-mass black holes. The simulation was performed preparing, again, the Brill-Lindquist-type of black holes as the initial data. The mass ratio was chosen as $q := M_1/M_2 = 1$, 1/2, 1/3, and 1/4 and initial coordinate separation as $2z_0 = 6.37r_S$. Gravitational waves of scalar mode with quantum numbers $l = 2$, 3, and 4 were extracted, and the radiated energy and momentum (and thus, the recoil velocity) are successfully calculated. The results are in a remarkable agreement with those of point particle approximation.[75] As q is decreased from unity, the recoil velocity reaches the maximum around $q \simeq 0.38$ to give $v_{\rm recoil} \simeq 12.8$km/s.

3.2.2. High-velocity collision of two black holes in $D = 4$

In this subsection, we briefly summarize the current status for the simulation of high-velocity collision of two black holes. The results in this type of simulations have been reported only for 4 dimensions. Although these are not the subjects of higher-dimensional numerical relativity, the 4D works could give an insight for higher-dimensional phenomena and deserve reviewing.

The first simulation for this issue was performed by Sperhake et al.[60] They simulated the head-on collision of two equal-mass black holes. The initial velocity was increased up to $v \simeq 0.94c$. They prepared the initial data of boosted black holes using the Brandt-Brügmann formalism (see §2.8). The energy E of each black hole was estimated as $E^2 = M_{\rm irr}^2 + P^2$, where $M_{\rm irr}$ is the mass estimated by the apparent horizon area, and the gamma factor γ as $E/M_{\rm irr}$. Because the Bowen-York initial data contains spurious radiation and its amount increases as γ is increased, the initial separation has to be sufficiently large to make the system relaxed in the early phase of the simulation (during which unphysical gravitational waves are emitted away). They found that as the Lorentz factor is increased, the amplitude of gravitational
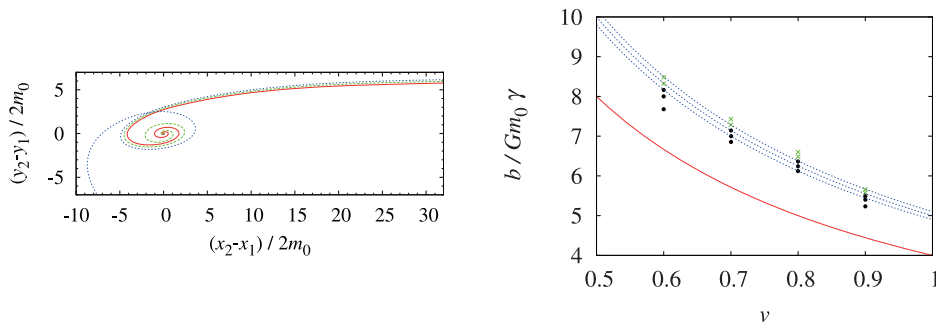
Fig. 6. Left panel: The trajectory of relative position of punctures for the impact parameter $b/Gm_0 = 6.0$, 6.2, and 6.4. Right panel: Summary of the outcome after the merger shown in the $(v, b/Gm_0\gamma)$ plane. The dots and crosses show the cases that two black holes merge or not. The figures are taken from Ref. 61).

waves emitted at the collision increases, and also, the contribution of higher-multipole modes becomes significant. The total radiated energy $E_{\rm rad}$ increases with γ, and by extrapolation, the value $E_{\rm rad}/2E$ was estimated to be $14 \pm 3\%$ in the limit $v \to c$.

The first simulation of high-velocity grazing collision of two black holes (i.e., collision with a nonzero impact parameter b) was performed by Shibata, Okawa and Yamamoto[61] using the SACRA code.[76] In this work, they prepared the initial data in a different manner from the Brandt-Brügmann formalism. Their idea is to first prepare the initial data of one boosted black hole by boosting a Schwarzschild black hole of mass m_0, and then, superpose those of two boosted black holes. Since there is an interaction between two holes, just superposing the two solutions causes the violation of Hamiltonian and momentum constraints. However, if the initial distance between the two holes is sufficiently large, violation of the constraints is small and hence may be ignored. Using such initial data, they simulated the off-axis collision focusing primarily on the threshold values of the impact parameter b for the black hole merger. The left panel of Fig. 6 shows the trajectory of relative position of two black holes for $v = 0.9$ and $b/Gm_0 = 6.0$, 6.2, and 6.4. Here, the positions of first and second black holes are given as $(x, y, z) = (x_1, y_1, 0)$ and $(x_2, y_2, 0)$, and the initial position of two black holes are $(x_{1,2}, y_{1,2}, z_{1,2}) = (\mp x_0, \mp b/2, 0)$. The black holes are scattered for $b/Gm_0 = 6.4$, while they merge for $b/Gm_0 = 6.2$. The right panel presents the summary for the outcome after the collision shown in the $(v, b/Gm_0\gamma)$ plane. The dots and crosses show the cases that two black holes merge or not. In 4 dimensions, we expect that the condition for the black-hole merger might be approximated by

$$\frac{J}{GM_{\rm ADM}^2} = \frac{bv}{4Gm_0\gamma} \lesssim 1. \tag{3.3}$$

Namely, if non-dimensional spin parameter of the system is smaller than unity, we may expect that two black holes merge. However, this is nothing but a weak sufficient condition. The right panel of Fig. 6 indicates that the condition for the black hole merger is approximately $bv/4Gm_0\gamma \lesssim 1.25$ for $v \to 1$. This value is by 50% larger than the condition for the apparent horizon formation in the collision of Aichelburg-
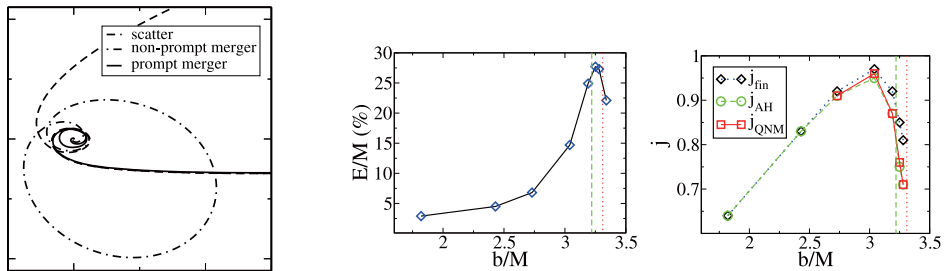
Fig. 7. Left panel: The trajectory of the puncture of one black hole for the impact parameter
$b/GM = 3.34$ (prompt merger), 3.39 (non-prompt merger), and 3.40 (scatter). Center and
right panels: The radiated energy E_{rad}/M and the rotational parameter $j = J_{BH}/GM_{BH}^2$,
respectively, as functions of the impact parameter b/M for initial velocity $v = 0.753$. The figure
is taken from Ref. 62).

Sexl particles at the instant of the collision,[20),22)] which gave $b/4GE \lesssim 0.84$ where
E is the energy of each incoming particle.

The radiated energy ΔE and angular momentum ΔJ were calculated from the
Newman-Penrose quantity, and it was evaluated as $\Delta E/M_{ADM} \approx 25 \pm 5\%$ and
$\Delta J/J_{ADM} \approx 65 \pm 5\%$, which are quite large values. As a result of the large angular-
momentum radiation, non-dimensional spin parameter of the system is significantly
decreased, and hence, black hole merger occurs even for $J/GM_{ADM}^2 \sim 1.25$. The
resulting black hole near the threshold value of b is a rapidly spinning Kerr black
hole with the Kerr parameter $a/M_{BH} \simeq 0.8 \pm 0.1$, where M_{BH} is the mass of the
resulting black hole.

The second simulation of high-velocity grazing collision of two black holes was
reported in Ref. 62) by the same authors of Ref. 60). They took close attention to
the "zoom-whirl" behavior which was not reported in detail in Ref. 61). Specifically,
they divide the impact parameter b into three regions: (i) $b < b^*$; (ii) $b^* < b < b_{scat}$;
and (iii) $b_{scat} < b$. The impact parameter in the region (i) leads to the immediate
merger, and that in the region (iii) leads to the scattering where two black holes
do not merge. In the region (ii), the merger does not occur in one encounter, but
the black holes rotate around each other several times ("whirls") where the radius
of the orbit sometimes becomes fairly large and eventually merge as a result of
gravitational-wave emission. The left panel of Fig. 7 shows the puncture trajectory
of one of two black holes for $b/GM = 3.34$, 3.39, and 3.40 in the case of initial gamma
factor $\gamma = 1.520$ ($v = 0.753$) and initial coordinate separation $d/GM = 174.1$. The
behaviors of the three cases (i), (ii), and (iii) are seen. The middle and right panels
show the radiated energy E_{rad}/M and the rotational parameter $j := J_{BH}/GM_{BH}^2$,
respectively, as functions of b/GM for the same initial gamma factor but for the
initial coordinate separation $d/GM = 62.4$. Here, j is estimated from quasinomal
mode frequency (QNM) and geometry of the formed apparent horizon. The resulting
value of J_{BH} was also compared with $J - J_{GW}$ (where J and J_{GW} are initial angular
momentum of the system and total radiated angular momentum by gravitational
radiation), and two values were checked to agree well. The radiated energy is $\simeq 23\%$
at $b \simeq b^*$ and the largest rotational parameter j is $\simeq 0.96$ for b slightly smaller

than b^*. They also performed simulations for the initial gamma factor $\gamma = 2.933$ ($v = 0.940$) and initial separation $d/GM = 23.1$. In that case, the radiated energy for $b \simeq b^*$ is $E_{\mathrm{rad}}/M = 35 \pm 5\%$, and the value of b_{scat} is $2.3 < b_{\mathrm{scat}}/GM < 2.4$. These values are slightly different from the results in Ref. 61): The radiated energy is larger and b_{scat} is smaller. This might be due to lack of the resolution of the former simulations or the different methods of initial data preparation.

In a recent paper, this work was extended by including spins of incoming black holes,[77] and the "superkicks" were studied in detail. They found that the kick velocity could be as large as 15,000 km/s, which is the largest value to date, and they conjectured the largest possible kicks in the two black-hole systems.

It is also worthy to point out a related paper by Choptuik and Pretorius[78] in which head-on collisions of two boson stars were studied. The motivation for this study comes from the fact that although the Aichelburg-Sexl particles or black holes are widely used in modeling the high energy particles in trans-Planckian collisions, how the elementary particles couple to gravity is quite uncertain and they might have to be treated as wave packets. As a classical model of colliding wave packets, they used the soliton-like configuration of minimally coupled scalar field ϕ, and simulated its head-on collision by changing initial gamma factor γ. The output of the collision depends strongly on γ, but the black hole formation was observed for $\gamma = 4$. This indicates that modeling the elementary particles in trans-Planckian collisions by point particles/black holes, as studied in Refs. 19), 20), 22), 60)–62), is valid at least at classical level.

3.3. *Bar-mode instability of Myers-Perry black holes*

The last topic in this chapter is the instability of rapidly rotating Myers-Perry (MP) black holes with one spin parameter.[25] The numerical-relativity simulations for this issue were performed in Refs. 28) and 29). The MP black holes have been inferred to be unstable against certain perturbations.[26],[27] Shibata and Yoshino for the first time clarified by fully nonlinear simulations that the MP black holes are indeed unstable if they are rotating sufficiently rapidly, and that the most unstable mode is the bar-mode.[28],[29] They also clarified the condition for the onset of the bar-mode instability quantitatively. In the following, we review their work.

3.3.1. The Myers-Perry black holes

In D-dimensional spacetimes, the spacetime can have $\lfloor (D-1)/2 \rfloor$ independent rotational parameters (i.e., the independent components of angular momentum tensor) where $\lfloor x \rfloor$ indicates the largest integer not greater than x. The black hole solutions of spherical horizon topology with arbitrary number of rotational parameters in higher-dimensions were found by Myers and Perry.[25] Hereafter, we consider only MP black holes with one spin parameter. The metric is given by

$$ds^2 = -dt^2 + \frac{\mu}{\Sigma}(dt - a\sin^2\theta d\varphi)^2 + \frac{\Sigma}{\Delta}d\hat{r}^2 + \Sigma d\theta^2 + (\hat{r}^2 + a^2)\sin^2\theta d\varphi^2 + \hat{r}^2\cos^2\theta d\Omega_{D-4}^2, \tag{3.4}$$

where

$$\Sigma = \hat{r}^2 + a^2\cos^2\theta, \tag{3.5}$$

$$\Delta = \hat{r}^2 + a^2 - \mu/\hat{r}^{D-5}. \tag{3·6}$$

In this case, the spacetime has a $U(1)$ symmetry with respect to the rotational plane and an $O(D-4)$ symmetry with respect to the directions orthogonal to the rotational plane. μ and a are related to the mass M and angular momentum J by

$$M = \frac{(D-2)\Omega_{D-2}\mu}{16\pi G}, \qquad J = \frac{2}{(D-2)}Ma. \tag{3·7}$$

The location $\hat{r} = r_K(M, J)$ of the event horizon is given by the equation $\Delta(r_K) = 0$. In 5 dimensions, the event horizon exists only for $a < \mu$, whereas it exists for any value of a for $D \geq 6$.

3.3.2. Previous studies

Here, the history for the stability analysis of the MP black hole is summarized. A standard method for this is a linear perturbation study. If the variables of the linear perturbation equations are separable, the resulting equation reduces to an ordinary differential equation and its analysis may be done analytically or semi-analytically. Although linear perturbation equations in the MP spacetime have been extensively studied for a metric perturbation, the separation of the variables was succeeded only for a tensor-mode perturbation.[79],[80] For other modes, the stability has not been found yet by this analysis.

The next best method may be to numerically solve partial differential equations for the linear perturbation equations without carrying out the separation of the variables. The first numerical analysis was done by Dias et al.[27] In this study, an axisymmetric perturbation (i.e. the perturbation that keeps the $U(1) \times O(D-4)$ symmetry) was studied and 2D simultaneous partial differential equations were solved. They clarified that the MP black hole with ultra high spin ($a \gg \mu^{1/(D-3)}$) can be unstable against axisymmetric deformation for the first time. However, no numerical study has not been done for nonaxisymmetric perturbation that breaks the $U(1)$ symmetry.

Alternatively, Emparan and Myers analyzed the stability of MP black holes using two different analysis methods.[26] In one analysis, they take the so-called black membrane limit of the ultra spinning MP black holes. The ultra spinning MP black holes for $D \geq 6$ with $a \gg \mu^{1/(D-3)}$ becomes extremely oblate. For such an extremely oblate black object, instabilities analogous to the Gregory-Laflamme instability is expected to set in. This discussion was applied to axisymmetric instabilities, and indeed, the numerical analysis of Dias et al. confirms this prediction.[27]

The other analysis was based on black-hole thermodynamics : They compared the horizon area of a rotating MP black hole with that of two boosted Schwarzschild-Tangherlini black holes, which recede from each other, fixing the total gravitational energy and angular momentum. The horizon area of a MP black hole is

$$A_{\mathrm{MP}} = \Omega_{D-2} r_K^{D-4} \left(r_K^2 + a^2 \right), \tag{3·8}$$

whereas sum of the area of two boosted black holes is

$$2A_S = 2\Omega_{D-2} r_S(m)^{D-2}, \tag{3·9}$$

where $r_S(m)$ is the horizon radius of a Schwarzschild-Tangherlini black hole. Here, the ADM mass M and the mass m of each black hole are related as $M = 2\sqrt{m^2 + p^2}$ where p is the magnitude of the momentum of each black hole. The angular momentum of the system J is given by $J = bp$, where b is an "impact parameter", i.e., the distance between two black holes in the direction orthogonal to the momenta and b is chosen to be $b \sim r_S(M)$ as a typical value. If $A_{\mathrm{MP}} < 2A_S$, the configuration of two boosted black holes may be preferred to the MP black hole thermodynamically. If this is the case, it is expected that the MP black hole becomes unstable against nonaxisymmetric perturbation, the horizon may pinch off, and the system may change to a state of two boosted black holes. By this discussion, the MP black holes are predicted to be unstable for

$$q := a/\mu^{1/(D-3)} \gtrsim \begin{cases} 0.85\,, & (D=5) \\ 0.96\,, & (D=6) \\ 0.99\,, & (D=7) \\ 1.00\,. & (D=8) \end{cases} \tag{3·10}$$

Here, we introduced a non-dimensional rotational parameter q which is used later. In contrast to the former discussion, this discussion can be applied to $D = 5$ as well as $D \geq 6$, and the predicted critical parameter for the onset of the instability is much smaller than that for the Gregory-Laflamme-like axisymmetric instability (i.e., the instability can set in for a smaller black hole spin). Therefore, the nonaxisymmetric perturbation was predicted to be the primary instability.

3.3.3. Setup of the problem

The prediction by Emparan and Myers seems to be qualitatively correct. However, for strictly verifying that the instability sets in and for quantitatively clarifying the criterion for the onset of the instability, we have to solve Einstein's equation, which can be done only by numerical-relativity simulation. To solve this problem, Shibata and Yoshino performed numerical simulations. In the following, we review their work.

The simulation was done in the following procedures. First, the MP black hole was written in the quasi-isotropic coordinates in which the radial coordinate is defined by

$$r = r_h \exp\left[\pm \int_{r_K}^{\hat{r}} \frac{d\hat{r}'}{\sqrt{\hat{r}'^2 + a^2 - \mu/\hat{r}'^{(D-5)}}}\right]. \tag{3·11}$$

This is analogous to the isotropic coordinates of the Schwarzschild-Tangherlini spacetime (i.e. the radial coordinate for which the spatial part of the metric becomes conformally flat), and the initial spacelike hypersurface possesses two asymptotically flat regions and one throat (i.e., the structure similar to the Einstein-Rosen bridge). In this quasi-isotropic coordinates, the horizon is located at $r = r_h$. This spacelike hypersurface does not cross the physical curvature singularity of the MP spacetime.
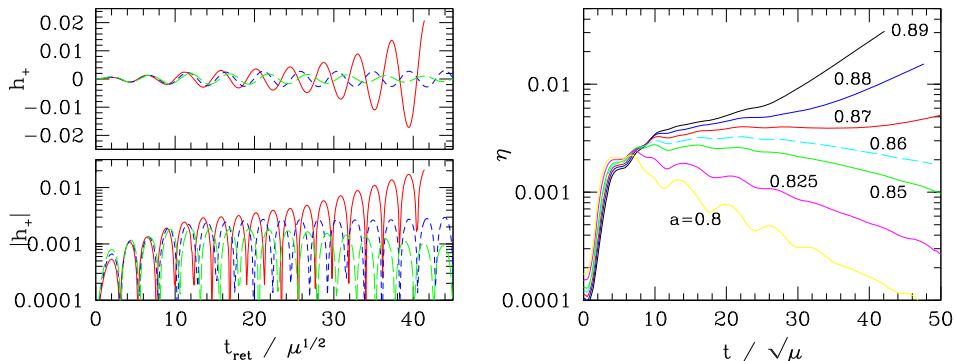
Fig. 8.   Left panel: h_+ and its absolute value as functions of retarded time for $a/\mu^{1/2} = 0.85$, 0.87, and 0.89 (dashed, long-dashed, and solid curves) in 5 dimensions. Right panel: Evolution of distortion parameter η of the apparent horizon for $q = 0.80$–0.89 in 5 dimension. The figures are taken from Ref. 28).

Then, the initial data is written in the (x, y, z, w_i) coordinates

$$x = r \cos\theta \cos\phi, \quad y = r \cos\theta \sin\phi, \quad \sqrt{z^2 + \sum_i w_i^2} = r \sin\theta, \qquad (3\cdot12)$$

where the (x, y)-plane corresponds to the plane of the rotation.

Next, a small nonaxisymmetric perturbation is added to the conformal factor of the BSSN variables, χ, as

$$\chi = \chi_0 \left[1 + A\mu^{-1}(x^2 - y^2) \exp(-r^2/2\hat{r}_K^2)\right], \qquad (3\cdot13)$$

where χ_0 is the value of unperturbed initial data, and A is a small number $\ll 1$. This perturbation breaks the $U(1)$ symmetry with respect to (x, y)-plane and keeps the $O(D - 4)$ symmetry with respect to z and w_i directions.

Adopting this initial data, Shibata and Yoshino evolved the system by SACRA-ND code, which is the generalized version of SACRA code.[76] This code employs the 4th-order finite differencing in space and the 4th-order Runge-Kutta method in time with an AMR algorithm. The modified version of the cartoon method explained in §2.2.2 is employed to impose the $O(D - 4)$ symmetry. For stable simulations, the parameters of gauge conditions (see Eqs. (2·48) and (2·49)) were carefully chosen (see Refs. 28) and 29) for details). One important finding on the dynamical gauge was that for unstable (rapidly rotating) black holes, a large value of η_β is favored in performing a longterm simulation until the growth of the instability saturates and subsequently the deformation damps.

3.3.4.   Numerical results

The left panel of Fig. 8 shows gravitational waveforms of $m = 2$ mode extracted in a local wave zone as a function of time for $D = 5$. For $q \lesssim 0.85$, the amplitude
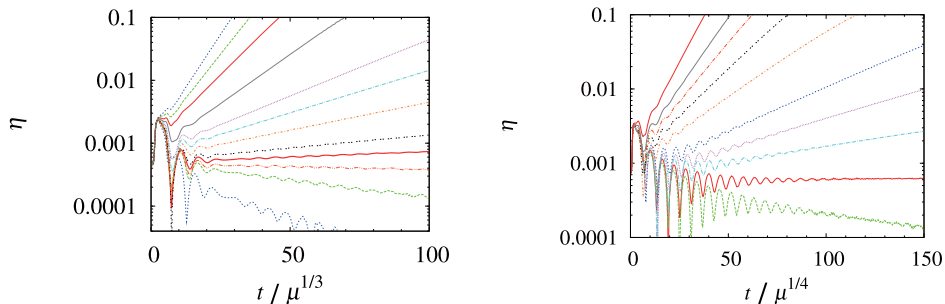
Fig. 9. Left panel: Time evolution of distortion parameter η for $D = 6$ and for the initial spin $q_i = a/\mu^{1/3} \approx 1.039, 0.986, 0.933, 0.878, 0.821, 0.801, 0.781, 0.761, 0.750, 0.740, 0.718$, and 0.674 (from the upper to lower curves) with $A = 0.005$. Right panel: The same as the left panel but for $D = 7$ and for $q_i = a/\mu^{1/4} = 0.960, 0.903, 0.844, 0.813, 0.783, 0.767, 0.751, 0.735$, and 0.719 (from the upper to lower curves). The figures are taken from Ref. 29).

exponentially damps with t. This shows that the black hole is stable. By contrast, the amplitude for $q \simeq 0.87$ remains approximately constant, and that for $q \simeq 0.89$ grows in time. This implies that for $q > 0.87$ the black hole is unstable against nonaxisymmetric deformation. The right panel shows the distortion parameter η. Here, η is defined by $\eta := [(l_0 - l_{\pi/2})^2 + (l_{\pi/4} - l_{3\pi/4})^2]^{1/2}/l_0$, where l_φ denotes the proper circumferential length between $\theta = 0$ and $\pi/2$ for a fixed value of φ evaluated on the apparent horizon. This parameter indicates the degree of deviation from the axisymmetry, and $\eta = 0$ for an axisymmetric surface. As can be seen, the value of η grows exponentially for $q \gtrsim 0.87$, while η damps for $q \lesssim 0.86$. This also shows that the rapidly rotating black hole with $q \gtrsim 0.87$ is unstable against nonaxisymmetric deformation. The critical parameter for the onset of the instability is $q_{\text{crit}} \simeq 0.87$.

Figure 9 shows the time evolution of the distortion parameter η for $D = 6$ (left panel) and 7 (right panel). Here, the definition of η is slightly modified as $\eta := 2[(l_0 - l_{\pi/2})^2 + (l_{\pi/4} - l_{3\pi/4})^2]^{1/2}/(l_0 + l_{\pi/2})$. As in the 5D case, the value of η exponentially damps in time if q is small, but it grows exponentially for q larger than a certain critical parameter q_{crit}. The value of q_{crit} is $\simeq 0.74$ and 0.73 for $D = 6$ and 7, respectively. The critical parameter q_{crit} for the onset of the instability is much smaller than that for the onset of the axisymmetric instability reported in Ref. 27) irrespective of dimensionality D. The results are summarized in Table II.

The solid curves of Fig. 10 plot gravitational waveforms in the longterm simulations where the initial value q is $q_i = 0.801$ (left panel) and 0.986 (right panel) for $D = 6$. The amplitude of gravitational waves grows in time and then saturates when the distortion parameter becomes of order 0.1 at $t = t_{\text{peak}}$. After the saturation, the amplitude exponentially damps. The reason is as follows. Associated with the growth of the nonaxisymmetric deformation, emissivity of gravitational waves is enhanced, and energy and angular momentum are significantly extracted from the black hole (although the area increases). As a result, the value of the non-dimensional spin parameter q is decreased, and eventually, it becomes $q \simeq q_{\text{crit}}$ when the growth of the amplitude saturates at $t = t_{\text{peak}}$. Gravitational waves continue

Table II. The values of critical rotational parameter q_{crit} of the onset of the bar-mode instability
for $D = 5$–8.

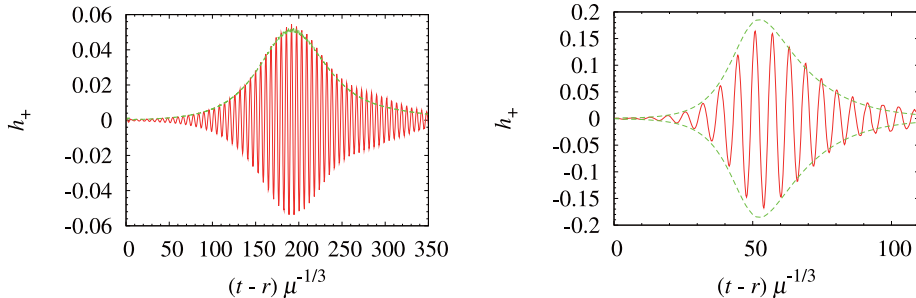| D	5	6	7	8
q_{crit}	0.87	0.74	0.73	0.77

Fig. 10. Left panel: + modes of gravitational waveform (solid curve) emitted from an unstable
black hole for $D = 6$ and for $q_i = 0.801$ as a function of a retarded time defined by $t - r$ where r
is the coordinate distance from the center. $\eta/2$ is also plotted as a function of t (dashed curve).
Right panel: The same as the left panel but for $q_i = 0.986$. The figures are taken from Ref. 29).

to extract energy and angular momentum even after the saturation and the final
state is a stable state with the value of $q = q_f$ which is smaller than q_{crit}. The time,
$t = t_{\mathrm{peak}}$, for $q_i = 0.986$ is smaller than that for $q_i = 0.801$. This is because the
growth rate of the instability for $q_i = 0.986$ is larger than that for $q_i = 0.801$, and
therefore, energy and angular momentum are extracted more efficiently. The dashed
curves of Fig. 10 plot half of the distortion parameter η of the apparent horizon.
It agrees approximately with the amplitude of gravitational waves, indicating that
the distortion of the apparent horizon is not due to a gauge mode and gravitational
waves are generated by the distortion of the system.

Figure 11 shows the real part of the gravitational-wave frequency as a function
of q for $D = 5$, 6, and 7. The line for the superradiance condition[81] $\omega \leq m\Omega_H$ is also
shown for each value of D, where $m = 2$ and Ω_H is the angular velocity of the horizon.
It is well known that the superradiance condition is the condition such that waves
can extract energy and angular momentum from a black hole without violating the
area theorem by Hawking (e.g., Ref. 23)). The superradiance condition is a necessary
condition for subtracting energy from the black hole by waves. However, it is only a
necessary condition and not the sufficient condition for the onset of the dynamical
instability found in Refs. 28) and 29). In the superradiance often discussed, one
considers to inject rather an artificial ingoing wave for which the frequency satisfies
this condition. For such an artificial wave, the reflected waves are amplified. For
the dynamical instability to occur, gravitational waves have to be spontaneously
excited by unstable quasinormal modes. Namely, such a mode has to satisfy not
only the superradiance condition but also the condition that the imaginary part of
the quasinormal mode is negative. Figure 12 shows the inverse τ^{-1} of the growth time
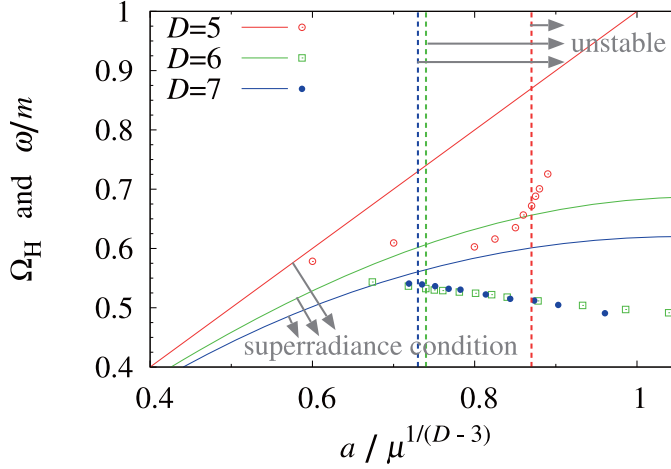scale of the instability for $D = 6$ (left panel) and 7 (right panel), which corresponds

Fig. 11. Real part of gravitational-wave frequencies ω/m (where $m = 2$) for selected values of the spin parameter for $D = 5 - 7$ (points) together with Ω_{H} as a function of $q = a/\mu^{1/(D-3)}$ for $D = 5 - 7$ (from the upper to lower solid curves). The units of the vertical axis are $\mu^{-1/(D-3)}$. The values $q = q_{\mathrm{crit}}$ for the onset of the bar-mode instability are also shown for $D = 5 - 7$ (from the right to left dotted lines). The figure is taken from Ref. 29) with modification.
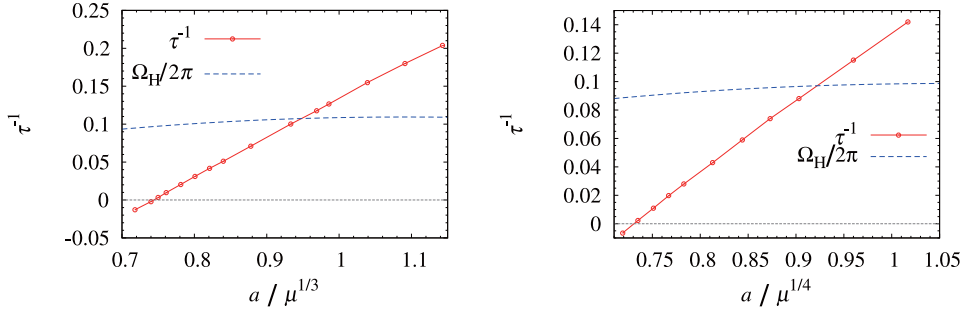

Fig. 12. Left panel: The growth rate $1/\tau$ of η in units of $\mu^{-1/(D-3)}$ as a function of q (solid curve) for $D = 6$. The dashed curve denotes $\Omega_{\mathrm{H}}/2\pi$. Right panel: The same as left panel but for $D = 7$. The figures are taken from Ref. 29).

to the imaginary part of the quasinormal modes. It indeed becomes negative for $q > q_{\mathrm{crit}}$.

The final state eventually reached after the onset of the bar-mode instability was also clarified in Ref. 29). For this purpose, the time evolution of the value of q was approximately followed by evaluating the degree of oblateness of the horizon, C_p/C_e, where $C_p = (l_0 + l_{\pi/2})/2$ and C_e is the proper circumferential length between $\varphi = 0$ and $\pi/2$ along the equatorial plane $\theta = \pi/2$ on the horizon. For a spherically symmetric surface, the value of C_p/C_e is unity, and it monotonically decreases as the spin of the MP black hole increases (as the oblateness of the horizon surface increases). In Ref. 29), the value of C_p/C_e was followed, and using the relation of
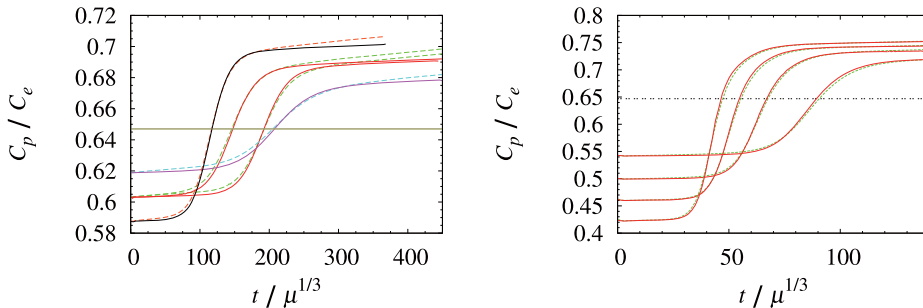
Fig. 13. Left panel: Time evolution of C_p/C_e for $D = 6$ and for non-dimensional spin parameters not much greater than $q_{\rm crit}$, $q_i = a/\mu^{1/3} = 0.821$, 0.801, and 0.781. The corresponding initial values of C_p/C_e are ≈ 0.587, 0.602, and 0.618, respectively. The results with $A = 0.02$ and 0.005 are plotted for $q_i = 0.801$, and the results with $A = 0.02$ are plotted for $q_i = 0.821$ and 0.781. The solid and dashed curves denote the results for $N = 50$ and 40, respectively, where N is grid numbers. The thin dotted line denote $C_p/C_e = 0.647$ which is the value of C_p/C_e for $q = q_{\rm crit}$. For $q_i = 0.821$, the simulation was stopped at $t/\mu^{1/3} \approx 370$ because the black hole reaches approximately stationary state. Right panel: The same as the left panel but for the large initial spins $q_i = 0.878$, 0.933, 0.986, and 1.039 with $A = 0.005$. $C_p/C_e \approx 0.542$, 0.499, 0.460, and 0.422 at $t = 0$, respectively. The figures are taken from Ref. 29).

$C_p/C_e(q)$, the spin, q, is approximately determined.

Figure 13 shows the value of C_p/C_e as a function of time. The value of C_p/C_e increases with time, indicating that the black hole spin decreases. Here, we focus on the curve starting from $C_p/C_e \simeq 0.62$, shown in the left panel. The initial value of q is $q_i = 0.781$, and the value C_p/C_e, which corresponds to $q = q_{\rm crit} = 0.74$, is shown by the dotted line. The curve crosses the dotted line at $t/\mu^{1/3} \simeq 200$, which agrees approximately with the time at which the growth of the gravitational-wave amplitude saturates. The final value of C_p/C_e is $\simeq 0.68$, and the corresponding value of q is $q_f \simeq 0.705$. Thus, a stable and moderately rapidly spinning black hole is the final outcome. Next, we focus on the curve starting from $C_p/C_e \simeq 0.42$ shown in the right panel. For $C_p/C_e = 0.42$, the initial value is $q_i = 1.04$. The value of C_p/C_e increases in time also in this case, and crosses the line for $q = q_{\rm crit}$. Then, it relaxes to a stable state with the value $C_p/C_e \simeq 0.75$, which corresponds to $q_f = 0.61$. Again, a stable black hole is the final outcome. It is interesting to note that for a high initial spin, the final spin is smaller.

To summarize, the MP black holes are unstable against nonaxisymmetric bar-mode deformation if they are spinning sufficiently rapidly. As a result of the onset of this instability, energy and angular momentum are extracted from the black hole by gravitational waves which are spontaneously excited by an unstable quasinormal mode.

It should be noted that Shibata and Yoshino could not follow the evolution of the black hole for $q_i \gg 1$. The reason is perhaps that the space structure for large value of q has a very long throat while the coordinate region to span this throat is limited, and hence, the resolution in space is not sufficient. Also, the growth of the

instability is very rapid, and this seems also to require a higher resolution. In this case, the horizon pinch-off might happen as discussed by Emparan and Myers,[26] and it is an interesting remaining issue to clarify the evolution of the instability for this parameter regime.

§4. Summary

In this chapter, we review the current status of higher-dimensional numerical relativity. As described in §2, the ingredients necessary for higher-dimensional numerical relativity have been prepared and many of interesting simulations are now feasible as in 4D one. In §3, we reviewed several simulations performed to date, which indeed showed that simulating interesting phenomena in higher-dimensional spacetimes is now feasible. A wide variety of extensions will be possible in the near future. For example, the simulation of unstable black objects such as black rings[82] is an interesting subject. The Gregory-Laflamme instability of a Kerr string and the dependence of the fate of the instability on the dimensionality D are also interesting. Among others, the high-velocity black hole collision seems to be the most important remaining issue to clarify the possible production rate of mini black hole in LHC.

In §1, we introduced AdS/CFT correspondence as one of the subjects for higher-dimensional numerical relativity. To study the issues of AdS/CFT correspondence applying numerical relativity, the formulations to handle the spacetimes with a negative cosmological constant $\Lambda < 0$ has to be developed. Although these have not been developed yet, the first step toward this direction was studied by Witek et al.[83] They simulated a spacetime of binary black holes by putting a timelike boundary at a finite distance, where the cosmological constant was set to be zero, $\Lambda = 0$. The motivation of this study comes from the fact that one of the specific features of AdS spacetimes is that spacelike infinity is timelike, and therefore, the artificial boundary at a finite distance is a good toy model that takes account of some features of AdS spacetimes. The formulations for handling $\Lambda < 0$ are also necessary for simulating black hole dynamics in the Randall-Sundrum braneworld scenarios. The formulation for such systems has been studied by Tanahashi and Tanaka (see Chapter 8).

Another interesting direction in the future is to develop formulations and codes for simulating spacetimes in Gauss-Bonnet gravity[84] (or, more generally, Lovelock gravity[85]). The Gauss-Bonnet gravity is a theory derived from a Lagrangian density with higher-order curvature terms, $\mathcal{L} = R + \alpha_{\mathrm{GB}}\mathcal{L}_{\mathrm{GB}}$ and $\mathcal{L}_{\mathrm{GB}} = R^2 - 4R_{MN}R^{MN} + R_{KLMN}R^{KLMN}$, but is a well-behaved theory in the sense that the third and fourth-order derivative terms of the metric do not appear in equations. Furthermore, the Gauss-Bonnet term is also predicted by low-energy limit of heterotic string theory. The $(N+1)$-formalism for Gauss-Bonnet gravity, which corresponds to the ADM formalism in general relativity, was developed by Torii and Shinkai.[86] However a numerically stable formulation has not been developed yet. Because the higher-curvature terms may become important in mini black hole production at accelerators and it causes a lot of interesting phenomena such as instabilities of spherically symmetric black holes,[87] exploring the dynamics of the higher-curvature theory will be an interesting and necessary subject.

References

1) F. Pretorius, Phys. Rev. Lett. **95** (2005), 121101.
2) M. Campanelli, C. O. Lousto, P. Marronetti and Y. Zlochower, Phys. Rev. Lett. **96** (2006), 111101.
3) J. G. Baker, J. Centrella, D. I. Choi, M. Koppitz and J. van Meter, Phys. Rev. Lett. **96** (2006), 111102.
4) P. Diener et al., Phys. Rev. Lett. **96** (2006), 121101.
5) F. Herrmann, D. Shoemaker and P. Laguna, gr-qc/0601026.
6) M. Boyle, D. A. Brown, L. E. Kidder, A. H. Mroue, H. P. Pfeiffer, M. A. Scheel, G. B. Cook and S. A. Teukolsky, Phys. Rev. D **76** (2007), 124038.
7) M. D. Duez, Class. Quant. Grav. **27** (2010), 114002.
   M. Shibata and K. Taniguchi, Living Rev. Rel. to appear (2011).
8) N. Arkani-Hamed, S. Dimopoulos and G. R. Dvali, Phys. Lett. B **429** (1998), 263.
9) I. Antoniadis, N. Arkani-Hamed, S. Dimopoulos and G. R. Dvali, Phys. Lett. B **436** (1998), 257.
10) L. Randall and R. Sundrum, Phys. Rev. Lett. **83** (1999), 3370.
11) L. Randall and R. Sundrum, Phys. Rev. Lett. **83** (1999), 4690.
12) J. M. Maldacena, Adv. Theor. Math. Phys. **2** (1998), 231; Int. J. Theor. Phys. **38** (1999), 1113.
13) M. Choptuik, L. Lehner, I. I. Olabarrieta, R. Petryk, F. Pretorius and H. Villegas, Phys. Rev. D **68** (2003), 044001.
14) D. Garfinkle, L. Lehner and F. Pretorius, Phys. Rev. D **71** (2005), 064009.
15) T. Banks and W. Fischler, hep-th/9906038.
16) S. Dimopoulos and G. Landsberg, Phys. Rev. Lett. **87** (2001), 161602.
17) S. B. Giddings and S. Thomas, Phys. Rev. D **65** (2002), 056010.
18) P. Kanti, Lect. Notes Phys. **769** (2009), 387.
19) H. Yoshino and Y. Nambu, Phys. Rev. D **67** (2003), 024009.
20) H. Yoshino and V. S. Rychkov, Phys. Rev. D **71** (2005), 104028.
21) P. C. Aichelburg and R. U. Sexl, Gen. Relat. Gravit. **2** (1971), 303.
22) D. M. Eardley and S. B. Giddings, Phys. Rev. D **66** (2002), 044011.
23) R. Wald, *General Relativity* (The University of Chicago Press, Chicago, 1984).
24) R. Gregory and R. Laflamme, Phys. Rev. Lett. **70** (1993), 2837.
25) R. C. Myers and M. J. Perry, Ann. of Phys. **172** (1986), 304.
26) R. Emparan and R. C. Myers, J. High Energy Phys. **09** (2003), 025.
27) O. J. C. Dias, P. Figueras, R. Monteiro, J. E. Santos and R. Emparan, Phys. Rev. D **80** (2009), 111701.
28) M. Shibata and H. Yoshino, Phys. Rev. D **81** (2010), 021501.
29) M. Shibata and H. Yoshino, Phys. Rev. D **81** (2010), 104035.
30) H. Yoshino, J. High Energy Phys. **01** (2009), 068.
31) T. Tanaka, Prog. Theor. Phys. Suppl. No. 148 (2003), 307.
32) R. Emparan, A. Fabbri and N. Kaloper, J. High Energy Phys. **08** (2002), 043.
33) R. Arnowitt, S. Deser and C. W. Misner, in *Gravitation: An Introduction to Current Research,* ed. L. Witten (Wiley, 1962), p. 227.
34) D. Garfinkle, Phys. Rev. D **65** (2002), 044029.
35) M. Shibata and T. Nakamura, Phys. Rev. D **52** (1995), 5428.
36) T. W. Baumgarte and S. L. Shapiro, Phys. Rev. D **59** (1998), 024007.
37) H. Yoshino and M. Shibata, Phys. Rev. D **80** (2009), 084025.
38) M. Zilhao, H. Witek, U. Sperhake, V. Cardoso, L. Gualtieri, C. Herdeiro and A. Nerozzi, Phys. Rev. D **81** (2010), 084052.
39) K. Maeda, M. Sasaki, T. Nakamura and S. Miyama, Prog. Theor. Phys. **63** (1980), 719.
40) F. Pretorius, Class. Quant. Grav. **22** (2005), 425.
41) L. Lehner and F. Pretorius, Phys. Rev. Lett. **105** (2010), 101102.
42) E. Sorkin, Phys. Rev. D **81** (2010), 084062.
43) L. Lindblom and B. Szilagyi, Phys. Rev. D **80** (2009), 084019.
44) R. Geroch, J. Math. Phys. **12** (1971), 918.
45) H. Witek, M. Zilhao, L. Gualtieri, V. Cardoso, C. Herdeiro, A. Nerozzi and U. Sperhake, Phys. Rev. D **82** (2010), 104014.
46) H. Witek, V. Cardoso, L. Gualtieri, C. Herdeiro, U. Sperhake and M. Zilhao, Phys. Rev.

D **83** (2011), 044017.
47) M. Alcubierre, S. Brandt, B. Brügmann, D. Holz, E. Seidel, R. Takahashi and J. Thornburg, Int. J. Mod. Phys. D **10** (2001), 273.
48) L. Smarr and J. W. York, Jr., Phys. Rev. D **17** (1978), 2529.
49) C. Bona, J. Massó, E. Seidel and J. Stela, Phys. Rev. D **56** (1997), 3405.
50) M. Alcubierre, B. Brügmann, P. Diener, M. Koppitz, D. Pollney, E. Seidel and R. Takahashi, Phys. Rev. D **67** (2003), 084023.
51) B. Brügmann, J. A. González, M. Hannam, S. Husa, U. Sperhake and W. Tichy, Phys. Rev. D **77** (2008), 024027.
52) K. I. Nakao, H. Abe, H. Yoshino and M. Shibata, Phys. Rev. D **80** (2009), 084028.
53) H. Kodama and A. Ishibashi, Prog. Theor. Phys. **110** (2003), 701.
54) L. D. Landau and E. M. Lifshitz, *The Classical Theory of Fields* (Pergamon Press, Oxford, 1962).
55) A. M. Abrahams and C. R. Evans, Phys. Rev. D **37** (1988), 318.
56) A. M. Abrahams and C. R. Evans, Phys. Rev. D **42** (1990), 2585.
57) A. M. Abraham, Phys. Rev. D **45** (1992), 3544.
58) E. Seidel and W.-M. Suen, Phys. Rev. Lett. **69** (1992), 1845.
59) H. Okawa, M. Shibata and K. Nakao, in preparation.
60) U. Sperhake, V. Cardoso, F. Pretorius, E. Berti and J. A. González, Phys. Rev. Lett. **101** (2008), 161101.
61) M. Shibata, H. Okawa and T. Yamamoto, Phys. Rev. D **78** (2008), 101501(R).
62) U. Sperhake, V. Cardoso, F. Pretorius, E. Berti, T. Hinderer and N. Yunes, Phys. Rev. Lett. **103** (2009), 131102.
63) H. Yoshino, T. Shiromizu and M. Shibata, Phys. Rev. D **72** (2005), 084020.
64) H. Yoshino, T. Shiromizu and M. Shibata, Phys. Rev. D **74** (2006), 124022.
65) D. R. Brill and R. W. Lindquist, Phys. Rev. **131** (1963), 471.
66) J. M. Bowen and J. W. York, Jr., Phys. Rev. D **21** (1980), 2047.
67) S. Brandt and B. Brugmann, Phys. Rev. Lett. **78** (1997), 3606.
68) I. Novikov, Ph.D. thesis (Shternberg Astronomical Institute, Moscow, 1963).
69) C. Misner, K. Thorne and J. Wheeler, *Gravitation* (W. H. Freeman and Company, San Francisco, 1973), p. 826.
70) F. Estabrook, H. Wahlquist, S. Christensen, B. DeWitt, L. Smarr and E. Tsiang, Phys. Rev. D **7** (1973), 2814.
71) T. W. Baumgarte and S. G. Naculich, Phys. Rev. D **75** (2007), 067502.
72) R. H. Price and J. Pullin, Phys. Rev. Lett. **72** (1994), 3297.
73) E. Berti, M. Cavaglia and L. Gualtieri, Phys. Rev. D **69** (2004), 124011.
74) G. T. Horowitz and K. Maeda, Phys. Rev. Lett. **87** (2001), 131301.
75) E. Berti, V. Cardoso and B. Kipapa, arXiv:1010.3874.
76) T. Yamamoto, M. Shibata and K. Taniguchi, Phys. Rev. D **78** (2008), 064054.
77) U. Sperhake, E. Berti, V. Cardoso, F. Pretorius and N. Yunes, Phys. Rev. D **83** (2011), 024037.
78) M. W. Choptuik and F. Pretorius, Phys. Rev. Lett. **104** (2010), 111101.
79) T. Oota and Y. Yasui, Int. J. Mod. Phys. A **25** (2010), 3055.
80) H. Kodama, R. A. Konoplya and A. Zhidenko, Phys. Rev. D **81** (2010), 044007.
81) S. A. Teukolsky and W. H. Press, Astrophys. J. **193** (1974), 443.
82) R. Emparan and H. S. Reall, Phys. Rev. Lett. **88** (2002), 101101.
83) H. Witek, V. Cardoso, C. Herdeiro, A. Nerozzi, U. Sperhake and M. Zilhao, Phys. Rev. D **82** (2010), 104037.
84) C. Lanczos, Ann. Math. **39** (1938), 842
85) D. Lovelock, J. Math. Phys. **12** (1971), 498.
86) T. Torii and H. Shinkai, Phys. Rev. D **78** (2008), 084037.
87) M. Beroiz, G. Dotti and R. J. Gleiser, Phys. Rev. D **76** (2007), 024012.